Electrical and optical characterization of nanostructured silicon oxide films for advanced photovoltaic applications

M. Morgano

December 19, 2011

Contents

1 Introduction **3**
1.1 The energy issue 3
1.2 PV limits 6

2 Nanocrystals for Photovoltaics **10**
2.1 Energy levels in QDs 10
2.2 Growth Techniques 11
2.2.1 Chemical Vapor Deposition 13
2.2.2 Sputtering 14
2.2.3 Relationship between stoichiometry and structural parameters 15
2.3 Transport in dielectric films 15
2.4 Doping of QDs 18

3 Samples description **22**
3.1 Single layer thick films 22
3.2 B-doped multi-layered films 24
3.3 Multi-layered films for electrical measurements 26
3.4 Samples for stoichiometry assessment 26

4 Optical characterization by IR spectroscopy **28**
4.1 Theory 28

4.2 Stoichiometry assessment 29
4.3 Identification of B-levels 36

5 Electrical transport in nanostructured Silicon dioxide films 40
5.1 Experimental setup 40
5.1.1 Samples preparation 40
5.1.2 Low temperature setup 41
5.1.3 High temperature setup 42
5.1.4 High voltage setup 43
5.2 Transport in films with different SRO stoichiometry . . 44
5.3 Transport in single layer thick films 50
5.4 Transport in B-doped multi-layered films 56
5.5 Transport in multi-layered films 62

6 All-silicon Quantum Dot-based Photovoltaic Device 69
6.1 Previous work 69
6.1.1 Deposition 69
6.1.2 Current-Voltage measurements 70
6.1.3 Optical characterization 70
6.1.4 Model describing the device 72
6.2 Experimental results 72

7 Conclusions 80

8 Acknowledgments 82

9 Publications list 83

Chapter 1

Introduction

1.1 The energy issue

It is a well known issue of the modern world the one regarding the not-sutainability of the energy demand. As of today the energy consumption exceeds by far the capability of its generation by renewable means. To make things worse, the so called *Hubbert Peak* appears to have been reached years ago and thus the oil availability is bound to steadily decrease and its price to steadily increase until it will be no longer economically viable to rely on such source to produce most of our energy.

There are several energy source that could be exploited in a renewable way and that do no contribute to greenhouse-gas pollution, but it is presently unclear whether these technologies combined could meet the ever-growing energy demand of the modern world. The most promising of these sources appear to be:

- hydroelectricity
- biomass

- geothermal
- ocean (from tides and waves)
- wind
- nuclear (fission and fusion)
- solar (thermal and photovoltaic)

Hydroelectricity is most likely the most mature technology, having been in use for the longest time of them. It is a very important energy source as of today, but the room for improvement are not too large. There also have been claims about whether it can be regarded as clean and not polluting or not given the high level of impact on the environment when building a dam and about the greenhouse gases released on the atmosphere from the sediments accumulating uphill the dam.

Biomass has been the primary source of energy for the humanity until the last century. It can be as efficient as oil and carbon burning but, unlike them, it is CO_2 neutral. The major drawback of this energy source is the amount of land required to make a true impact on a global scale. The impression is that this requirement is very strict and it is unclear wether this land should be used for food plantation or for specific cultivation that has the most yield with respect to biomass production.

Geothermal energy is the result of the earth core cooling down from its molten state and the heat produced by the decay of radioactive materials in the earth crust. There are two ways to exploit the higher temperature deep below the surface: the production of electricity with a geothermal plant or by using it to heat houses. The first is possible only where the heat flux is high enough to be useful. Such hot spots, located near hot springs, are rare and only a few countries could exploit

them regularly, but without making a real difference on a global scale. Using heat pumps to heat houses, while not directly a source of electric energy itself, could provide, instead, an important way to reduce the total energy demand on a global scale.

Energy from the oceans can be extracted from tides and from waves. Tidal energy can be exploited pretty much as a form of hydroelectricity, but with barrages that get filled every 12 hours. Energy form ocean waves can be extracted from their motion. The drawback of this form of energy is that the operational cost to maintain working turbines in an extremely corrosive environment such as sea water can be severe, furthermore not every countries has coastlines and particularly, not ones with useful tides excursion.

Wind energy appears to be a serious candidate to fill a substantial part of the energy demand for the future. Today's turbines are much more efficient than past ones and they also feature a lot less downtime. The energy potentially generated is huge and able, in theory, to fill by itself all the energy needs of today's and tomorrow's economy. Leaving aside the fact that the deployment of a huge number of turbines requires a huge amount of material for building them, the biggest problems of this kind of energy source is its intermittency (which would require the design of an intercontinental power grid to fill the gaps of a nation with the energy of another nation) and the inherently low density (10 W/m^2 being a very high figure). Nevertheless this is appears to be a promising energy source.

Nuclear power from the fission of high-Z nuclei is a greenhouse -free source of energy (not taking into account the mining of uranium ore) and with very high energy density (comparable with thermoelectric plants). With the current technology, it is not a renewable source since the supply of uranium is limited and somewhat scarce, projected to last for the next 50 years if used at a rate that has to meet the energy growth demand. Future generation approaches, such as self breeders, still have to prove their feasibility but could in principle

solve the energy problem. Anyway since nuclear energy is perceived as dangerous and the problem of nuclear waste is a hot (and still unresolved) one, at the moment this does not seem to provide a viable alternative to fossil fuels. Moreover, nuclear power from the fusion of light elements is still experimental, even though this would probably provide the solution to all the energetic needs in the future.

Lastly, solar energy can be used in two ways: thermodynamic and photovoltaic. While the first one can be used to ease the burden of the electricity demand to the grid or to store energy and use it overnight (with molten salt for example), the first one appears to be the most promising. On the earth surface every hour shine enough light that, if converted in energy, could meet the energy demand of one year. It has been shown that covering one tenth of the Sahara desert with commercially available photovoltaic (PV) modules could provide the energy needed worldwide. It is also carbon free and in practical terms unlimited. One of the biggest drawbacks is again, the intermittency. At night, no energy is generated and, when cloudy, there is a severe cut in the energy production. Another very important characteristic that holds the PV energy back is its very high cost compared to the other means of production. Nevertheless it would be difficult not to see PV energy as a major possible energy source of the future. The main parameter upon the question whether PV will be able to meet the energy demand or not can be answered is the efficiency of a module. With the present technology, this efficiency is limited for physical reasons and can not be enhanced much by normal industrial means (such as using more pure material). New approaches are being used to try and overcome these limitations.

In this thesis I will show the results of my research in the field of advanced photovoltaics, a very hot and recent topic that can have major impact on the future of energy production.

1.2 PV limits

If an important fraction of the energy demand is to be generated by photovoltaic cells, it is mandatory to address its key problems. A key issue of PV cells is the cost per unit area or per unit of Watt-peak produced. Both these values are tightly linked together and both stems from the value of the efficiency of the cell itself which the fraction of the power of the incident light that is converted into electricity. Increasing this value (retaining the cell cost fixed) will lower the area of land demand thus reducing the cost per unit area and will increase the power produced further reducing the cost per unit of watt-peak. It has been shown [1], however, that the efficiency of a standard, single-junction solar cell has an upper limit that depends only on the value of the energy gap (E_g) of the semiconductor and that, under standard illumination (air mass 1.5), has a maximum of around 31% for $E_g \sim 1.2$ eV. Silicon has a $E_g = 1.12$ eV which is already close to the optimum. The record efficiency of a Si solar cell is $\sim 25\%$ [2] which is already remarkably close to its theoretical limit and further major improvements are deemed not plausible without increasing substantially the cost. Furthermore, because of the not perfect matching between the currents and of ohmic losses, a module always perform worse than its cells. The reason of this limit stems from the competitive processes that happen in a semiconductor. Photons of energy less than E_g are not absorbed because they cannot promote an electron from the valence band to the conduction band. If this was the only process happening in the cell, decreasing the band gap would increase the efficiency because more photons can generate a pair of electron-hole increasing the short ciruit current (I_{SC}). But each exciton generated by a photon, contributes to the open circuit voltage (V_{OC})of the cell by E_g/e (where e is the elementary charge). Since the power generated is proportional to the product of these values, there must be a balance and a optimum value of the band gap that maximize

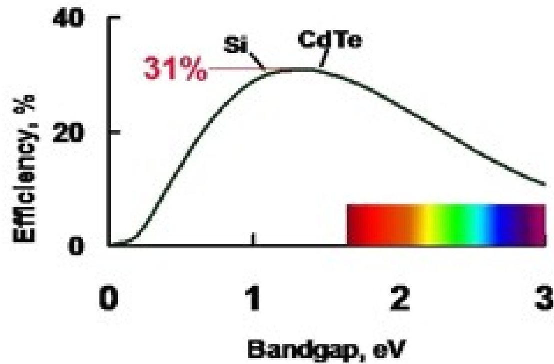

Figure 1.1: Shockley-Quaisser efficiency limits as a function of band-gap.

the efficiency. For the solar spectrum at mid-latidues this is, as said before, 31 % for $E_g \sim 1.2$ eV (Fig. 1.1). To circumvent this limit, it is necessary to relax the assumption that Shockley and Quaisser made for their calculation. The most obvious one to drop is the assumption of having a single junction [3]. By stacking another cell on the top (the side where the light comes from) of one cell featuring a lower E_g, it is possible to convert an bigger portion of the solar spectrum: the top cell will convert high energy photons while the bottom one will convert the radiation that cannot be absorbed by the first device (Fig. 1.2). By doing this and by carefully choosing the values of the E_g of the two cells it is theoretically possible to boost the efficiency up to 42%. It is not necessary to stop with two cells, but other addition will have diminishing returns. With 3 cells the (theoretical) efficiency would be 49%, with 6, 58% and with an infinite number of cells, all carefully tailored, the efficiency can go as high as 68% (Fig. 1.3). The obvious

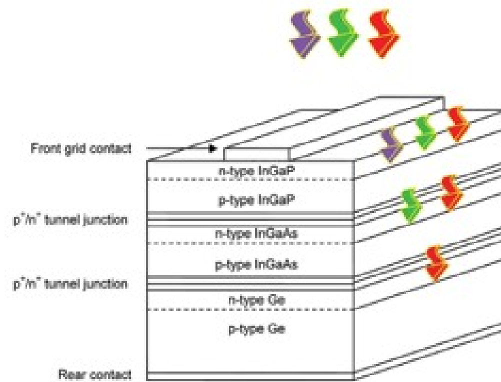

Figure 1.2: Schematic design of a tandem solar cell.

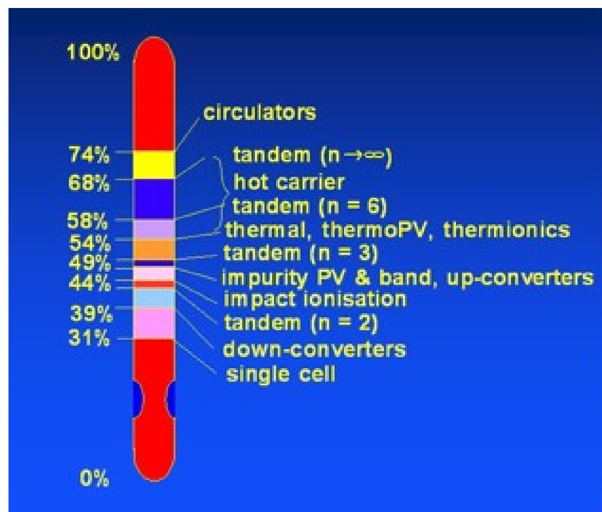

Figure 1.3: Calculated maximum theoretical efficiencies for various scenarios.

limitation of this approach is the cost. Since several independent cells of different material are needed, the cost of each one adds up, not counting the optical and electrical coupling of all of them. Moreover, it is not granted that the choice of the material is optimal since the energy gaps are fixed for each material and there might be a lack of a particular optimum value. This consideration lead to the approach called of 3rd generation.

The standard, single junction, mono- or multi- crystalline silicon solar cells are referred to as 1st generation solar cells, since those are the ones developed first. They are, at the moment, the most widespread of all PV technologies (accounting for $\sim 90\%$ of the market), they are reliable and durable and consistently achieve module efficiencies of $\sim 18\%$. Their major drawback is their very high cost. Silicon is a very expensive and energy-intensive material and its required at relatively high thickness $\sim 200\mu m$ since it is also indirect-bandgap. Another drawbacks is the stiffness: they can not be bended and used for building integrated photovoltaics.

To overcome these limitations, it has been proposed a new paradigm for PV cells, the so called 2nd generation. These cells employ a thin-film approach and new materials to severely lower the cost. These cells use less material ($\sim 100nm$ of thickness) and are often able to be deposited on various kind of substrates, also flexible ones. This approach cut the cost, but the efficiency is usually lower than the one in Si solar cells. They also often use rare and polluting elements such as Cd, Te and In.

The 3rd generation approach aims to merge the positive features of both 1st and 2nd generation: using less and less rare material to lower the cost while keeping the efficiency as high as the one in Si or even more. To do so it is necessary to rely on different physical concept and to employ Si technology, which is well developed, robust and uses non-toxic and non-rare material.

By exploiting nanotechnologies and concepts typical of the nanoscale,

it might be possible to engineer the band gap of a silicon based material almost at will thus allowing the deposition of different active layers stacked on top of each other using the same precursors (already widely available and widespread) on silicon building an all-silicon tandem solar cell.

My doctorate thesis is about the electrical and optical characterization of such nanostructured films and will be the resume of the research activities both at the University of Milano-Bicocca, Materials Science department within MIBSolar and at University of New south Wales, at the School of Photovoltaic and Renewable Energy Engineering within the Photovoltaic Centre of Excellence.

Some samples also come from Fondazione Bruno Kessler (FBK) in Trento, a research centre we collaborate with for the deposition and the characterization of sample deposited with a different technique than the ones from Sydney.

Chapter 2

Nanocrystals for Photovoltaics

2.1 Energy levels in QDs

As mentioned earlier, the efficiency of a silicon-based solar cell is bound to be under $\sim 30\%$. Its cost is also a drawback for the widespread, environment friendly use of Si solar cell as the main energy source worldwide. However, silicon has a very clear advantage over other materials, being the second most common element in the earth crust and being its technology the most well developed, reliable and studied. To maintain these advantages and try to push the efficiency further, one has to rely on more complex physical concept.

The underlying concept to be exploited is the engineerization of the band structure of the material to better fit the desired parameter or to create on the same substrate regions with different band structure. This of course can not be done with a bulk material whose parameter are fixed by the material itself, but one need to effectively create a 'new' material. Bearing in mind that the band structure of a solid is

the result of the degeneration of the levels of the constituent atoms superimposing to each other, the building block of the new material must be a well reproducibly unit with energy levels spaced apart and tunable at will. The superimposition of these (all equal) energy levels will form a band structure that will be able to be fitted (if the levels are tunable) to the desired shape. By confining an electron in a potential well it is possible to obtain a discrete energy spectrum which is fully determined by the width of the well. By forming an array of equally spaced three-dimensional wells the levels will merge into a band structure that depends only on the width of the wells. Lastly, if the dimension of this well is in the nano-scale, the energy of the levels and of the gap that will form is suitable for photovoltaic use. Such a well is called quantum dot (QD) and can be built by forming a nanocrystal of silicon embedded in a dielectric matrix. In such a system the energy level of the electrons will be [4]:

$$E_n \simeq 3\frac{\pi^2\hbar^2}{m^* a^2} n^2 \Bigg/ \left(1 + \frac{2\hbar\sqrt{2m^* V_0}}{a}\right)^2 \tag{2.1}$$

where E_n is the n-th energy level, m^* is the (reduced) mass of the carrier, a is the size of the cubic dot and V_0 is the potential barrier between the dot and the matrix and $\hbar$ is the reduced Plank constant.

A QD-based solar cell will take advantage of these levels obtained by quantum confinement and engineer the band gap by superimposing a number of them with different spacing, making it possible to tune the band gap of the bulk material. Thus, different layers with different band gaps can be achieved by using a mixture of quantum dots of different sizes and spacings for harvesting the maximum proportion of the incident light. One of the most promising technological improvement is to obtain this nanostructuration by thin film silicon-based processes in order to assemble an all-Si tandem solar cell. The use of silicon is also convenient because a standard Si solar cell provides an

almost optimal band gap for use as the bottom cell in a stack of two or even three solar cells in a tandem (Fig. 2.1).

With this choice, the theoretical efficiency limits are, respectively 42% (with the top cell having a band gap of 1.7 eV) and 47.5% (with band gaps of 1.5 and 2.0 eV for the middle and the topmost cell, respectively) [5].

As for the extraction of the current, this material is expected to have a high resistivity, unless it is so carefully prepared that the QDs are of the same dimensions and spacing. If this condition is met, then the charges might be able to travel through the cell by *Resonant Tunnelling* (as explained later) and loose only a fraction of the energy. If, however, the sample cannot be defined so precisely (which is likely, due to the fundamental stochastic process that controls QDs formation), it is not impossible to be able to successfully use the solar cells, provided that, whatever the transport mechanism is in place, the efficiency is higher than a c-Si solar cell.

2.2 Growth Techniques

Si nanocrystallites can be fabricated by depositing an over-stoichiometric dielectric material with an excess of silicon. After the deposition, a high temperature anneal may be required to allow the precipitation of the excess silicon and the formation of Si nanocrystals. Such a material has been studied also for its use for high quality memory device [6] [7] [8] and electroluminescent device [9] [10] [11].

If needed, the control of the size of the nanocrystals can be achieved by the deposition of a multi-layered structure where the silicon-rich material is alternatively deposited with a stoichiometric one, as shown in Fig. 2.2, that act as a diffusion barrier and force the excess silicon to segregate only in the silicon rich layer, up to the size of the layer itself. Fine control of QDs sizes can be achieved in this way. The idea

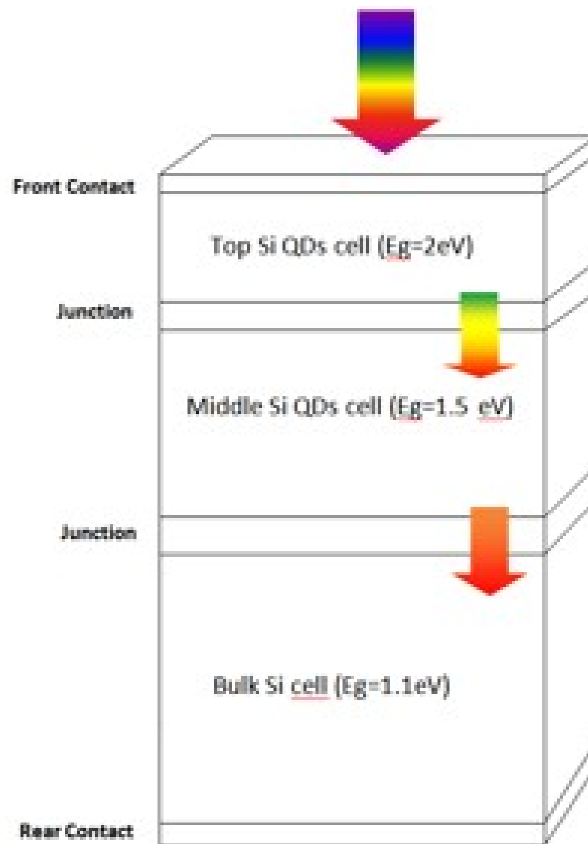

Figure 2.1: Proposed design for an all-Silicon tandem solar cell.

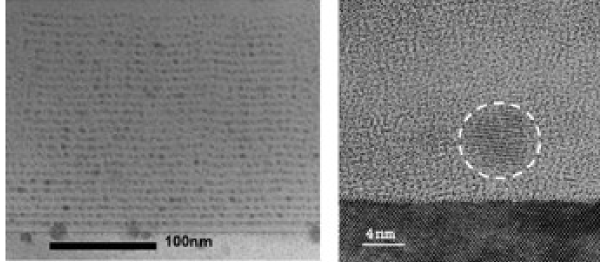

Figure 2.2: TEM images of a multi-layered nanostructured SRO structure (left) and of a single nanocrystal (right).

is that the over-stoichiometric mixture of silicon and oxygen (Silicon Rich Oxide - SRO) or silicon and nitrogen (Silicon Rich Nitride - SRN) upon annealing will segregate according to the relationship:

$$SiO_x \rightarrow \frac{x}{2} \cdot SiO_2 + \left(1 - \frac{x}{2}\right) \cdot Si \tag{2.2}$$

with an obvious analogous one for nitride.

While this has been showed to be an over-simplification [12], it's however a good first approximation start as can be seen from the data of photoluminescence (PL) in Fig. 2.3, starting to fail only at small diameters. Two main thin-film techniques have been exploited for the deposition of such material, Chemical Vapour Deposition (CVD) and sputtering.

2.2.1 Chemical Vapor Deposition

In the CVD technique [13] [14], the substrate (Silicon or quartz in the case of the samples used in this thesis) is heated at $\sim$ 200°C in vacuum and fluxes of silane (SiH_4) and nitrous oxide (N_2O) are let in the chamber. At the surface of the substrate occur a chemical

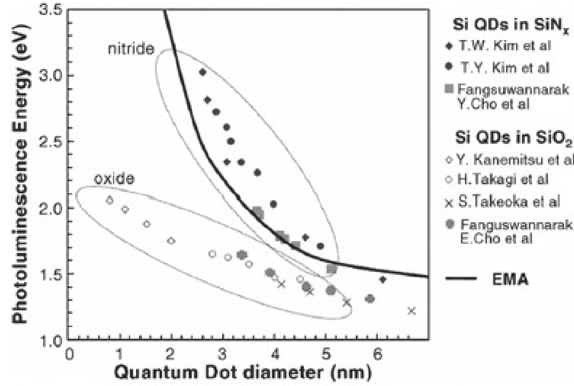

Figure 2.3: Measured (dots) and calculated (lines)PL energy as a function of dot diameter.

reaction where the silicon reacts with the oxygen yielding a silicon oxide and the nitrogen reacts with the hydrogen yielding ammonia which evaporates. By varying the fluxes of the two gases it is possible to vary the stoichiometry, but the relationship is not easy to calculate. Also, with this technique, the presence of nitrogen in the chamber implies unavoidable inclusions of oxynitride of silicon in the film. To deposit non-stoichiometric SRN instead of nitrous oxide it is possible to use ammonia (NH_3), but the oxygen in the residual atmosphere in the camber will still lead to the inclusion of some oxide in the film.

The sample prepared by the Fondazione Bruno Kessler (FBK) for this thesis are made with this technique and, as explained in more details later, are characterized by the ratio of the fluxes of N_2O vs. SiH_4 with the parameter 'Γ': $\Gamma = \frac{[N_2O]}{[SiH_4]}$.

2.2.2 Sputtering

Sputtering is another thin-film deposition technique that takes advantage of the 'spraying' of the atoms of a target when hit by a ions bombardment. They then fly balistically onto the target where they remain and form the film. By employing multiple targets it is possible to vary the stoichiometry of the deposited film: depositing together stoichiometric silicon dioxide and silicon a SRO will effectively be deposited on the target. With this method it is achievable a good control of the thickness and of the stoichiometry, as well as being very easy to deposit multi-layered structures. The deposition rate for each target is, in fact, proportional to the voltage applied to the target for a wide range of values and by shutting down the power to a target immediately cut off the deposition of that material. To vary the stoichiometry it is necessary to modify the voltage applied to the silicon target, while keeping the one for silicon dioxide fixed. Once one reach the desired thickness for the SRO layer, it is just necessary to shut off the silicon target to be able to deposit the silicon dioxide interlayer. If it is necessary to dope the layers, one just have to turn on the dopant target.

The samples prepared at the University of New South Wales are deposited in this way, and in some case another target is added to the two we mentioned earlier to deposit the 'dopant' atoms.

2.2.3 Relationship between stoichiometry and structural parameters

The possibility of the tuning of the band gap of such a material is strongly dependent on the ability to grow quantum dots of homogeneous dimensions and spacing. The two parameters that can be varied during the deposition (stoichiometry and layer thickness) fully define the structural parameters of the quantum dot at the random diffusion

scale. Upon annealing the excess silicon precipitates and nucleates quantum dots whose size is constrained to be between two silicon dioxide layers that, as said earlier, act as diffusion barriers. Thus the thickness of the SRO layer determines the dimension of the QD. The amount of silicon in excess that can segregate (the over-stoichiometry) determines the density of the dots and thus the spacing [15]. It has been shown, however, that also the annealing method plays a role in the determination of the size, with longer and higher temperature annealing resulting in slightly bigger QDs but with a plateau when the annealing is very long [16]. For thick, single layered SRO samples, there is no constrain on the size of the dots (other than, obviously, the layer thickness itself) and thus the relationship between size, spacing and stoichiometry depends strongly on the annealing procedure. As expected, low stoichiometry tends to yield smaller and scarcer QDs with respect to samples with higher silicon excess for a given annealing procedure. On the other hand, for a given stoichiometry, an annealing that lasts longer or at higher temperature will results in bigger QDs than a milder one. Lastly, it has been shown in [17] that a dispersion in the dot sizes has a greater effect in worsening the conductance than that in dot spacing because the shift in energy level from dot to dot quickly jeopardize the interference far more than the different exponential decay of the wavefunction from different thicknesses. This is an important factor for the film growth, as the thickness of the SRO layer (and hence the QDs size) can be controlled fairly precisely, unlike the spacing between them which is essentially due to a stochastic process.

2.3 Transport in dielectric films

A significant part of this research has been devoted to the identification of the effect of the nanostructuration and of the ordering of

the QDs over the electrical transport mechanism. The collection of charges in SRO is especially difficult because the QDs are dispersed in a dielectric matrix which act as insulator, hindering the flow of the current and its extraction from the electrodes. To identify the changes in the conduction mechanism, we employed a technique that consists in collecting the current-voltage characteristics of the samples at different temperatures and then identify a parameter that is known with a good precision. We then try to fit the current-voltage curves and calculate from the fits the chosen parameter. If the calculated value is compatible with the correct one, then the process used for the fitting procedure can be assumed to be the one really happening in the sample. It is to be noted, however, that we cannot expect a very precise agreement between the values, because the equations of the models tend to describe idealized situations and also because there can be more than one process at work at the same time.

The processes that we considered for these samples are typical of the conduction through dielectric films. This is because SRO itself is an insulating material and, when annealed, it forms a nanostructured film with QDs dispersed in a dielectric matrix of SiO_2. The mechanisms that we considered are the following ones:

- Schottky emission
- Poole-Frenkel effect
- Fowler-Nordheim emission
- Trap Assisted Tunnelling
- Hopping
- Resonant Tunnelling

Schottky emission [18] is the injection to the conduction band of a dielectric material of a carrier that gains enough energy to overcome the potential barrier between the metal and the insulator. This is, obviously, a thermally activated process and has the expression (Eq. 2.3):

$$J = A^* T^2 \exp\left(-\frac{q\left(\Phi_B - \sqrt{\frac{qE}{4\pi\epsilon_i}}\right)}{k_B T}\right) \tag{2.3}$$

where J is the current density, A^* is the effective Richardson constant, T is the absolute temperature, q is the electric charge of the electron, Φ_B is the barrier height, E is the electrical field, ϵ_i is the dielectric constant of the matrix and k_B is the Boltzmann constant.

From this equation we can calculate the dielectric constant of layer and compare it with the real value from literature. It has to be noted that, while for non-nanostructured SRO layer the value of the electrical field can be quite safely assumed as $E = V/d$ (where d is the thickness of the layer) this assumption could be wrong in the case of nanostructured material, since it is not clear which d to use, if the entire thickness, the mean dot spacing, the minimum spacing and so on.

Poole-Frenkel (PF) [19] [20] effect is a thermoionic emission from the valence band of a dielectric material to its conduction band enhanced by the band bending due to the polarization. The electron, therefore, needs less thermal energy with respect to the case of Schottky emission, since some of the energy needed is provided by the electrical field across the insulator. The expression is as follows (Eq. 2.4):

$$J \propto E \exp\left(-\frac{q\left(\Phi_B - \sqrt{\frac{qE}{\pi\epsilon_i}}\right)}{k_B T}\right) \tag{2.4}$$

with the same meaning of the symbols as before.

Again, we calculate from this equation the dielectric constant of the matrix. A slight modification has been proposed to this expression, that will be discussed it further in the following paragraph 5.3.

Fowler-Nordheim (FN) [21] [22] emission is the emission through a dielectric material of electrons induced by a high electrical field. This is essentially a tunnelling process that could not happen for the entire thickness of the barrier layer, but that is possible because the electrical field-induced bending of the (now essentially triangular) bands allows for the tunnelling of the electrons through an apparent effective thinner layer. Its expression is as follows (Eq. 2.5):

$$J = \frac{q^2 m_0}{8\pi h m^* \Phi_b} \frac{V^2}{d} \exp\left(-\frac{8\pi\sqrt{2qm^*}d\Phi_B^{3/2}}{3hV}\right) \tag{2.5}$$

with h being the Planck constant and m^* the effective mass of the electron.

From this equation we can calculate the barrier height of the dielectric layer, but the effective mass of the electron in the medium must be known.

Trap-Assisted Tunnelling (TAT) [23] is the mechanism of successive tunnelling processes for electrons with not enough energy to overcome the full bandgap at once, but that can be injected to the conduction bands via trap states localized in the forbidden band. The expression is (Eq.2.6):

$$I \propto \exp\left(-\frac{\pi d\sqrt{2qm^*}}{3hV}\Phi_B^{3/2}\right) \tag{2.6}$$

with I and$V$ being the current and the voltage drop respectively.

again from this equation, the potential barrier height can be calculated, assuming the effective mass of the electron to be known.

Hopping [24] is a process that, in principle, could very well be fit with the structure of nanostructured SRO, since it describes the transport of a carrier that tunnels a short distance through an insulating

matrix, passing from conductive grain to conductive grain dispersed more or less randomly but, in overall, uniformly. The conductance in such a case has a peculiar dependence with the temperature (Eq. 2.7):

$$G = G_0 \exp\left[-\left(\frac{E_{act}}{k_B T}\right)^{1/2}\right] \tag{2.7}$$

with G andG_0 being the conductance and the base conductance respectively.

Finally, *Resonant Tunnelling* [25], cam be thought as a generalization of the way carriers move in a real solid. When a number of levels with the same energy are brought close together, the degeneration of this systems lead to the formation of a band structure where only certain energies are allowed to tunnel from a centre to the other. In such a system, the current-voltage characteristics would feature a negative differential resistance (NDR) at voltages corresponding to the resonant energies.

2.4 Doping of QDs

It's widely known that one of the basic requirement for a PV cell is the ability to collect the electron and the hole created by a photon: i.e. there need to be a junction with a built-in electric field. There are two ways to incorporate nanostructured SRO arrays to form a junction whose V_{OC} is determined by the nanostructured material. They can be placed as an absorbing material sandwiched between a p-type and an n-type semiconductor with a larger or equal band gap of the absorbing material (thus creating a sort of p-i-n junction) or they can be part of a distributed p-n junction themselves with layers of opposite type of QDs. This approach requires the ability to dope the QDs so they can be used to create a junction. The second solution appears to be easier,

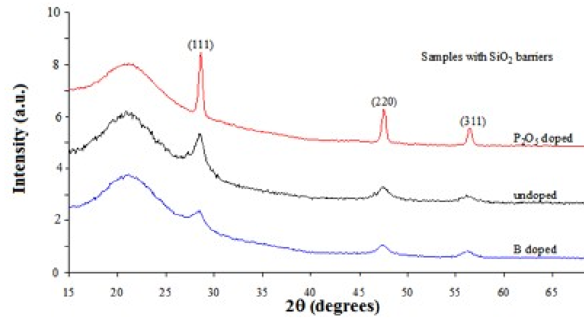

Figure 2.4: XRD spectra of samples with different levels of doping showing the effects of dopants on QDs dimensions.

provided that it is even possible to dope QDs, since it does not involve the electrical transport through a substantial thickness of dielectric. To follow this route, it is necessary to choose elements that feature high solid solubility in Si. Phosphorous and boron [26] are excellent candidates for this, and they are also already extensively used to dope bulk silicon. Its noteworthy to point out that to have a dopant density of $10^{18}cm^{-3}$ given the small size of a QD (typically containing 500-1000 atoms) less than one dopant atom per QD is required, which poses serious problems of uniformity. To deposit and at the same time dope QDs multilayers, the cosputtering technique can employed. Targets of P_2O_5 and pure B are used as the source of dopants: the variation of the deposition rate controls their concentration. Concentrations up to 0.5 at.% [27] have been used so far. It is therefore clear that cosputtering technique used to achieve doping, uses far higher concentration than the required one leaving no doubt that most of the incorporated atoms are inactive [28]. XRD and Transmission Electron Microscopy (TEM) measurements have been performed on doped samples and are reported in Fig. 2.4. For P doping a larger crystal size with respect to

undoped samples has been observed, so large that at 0.5 at% the size of the nanocrystals was almost double than in the reference sample. This occurrence, combined with the fact that the crystals formation starts at lower temperature for P-doped material, leads to the conclusion that P atoms enhance the crystallization of the Si nanocrystals. The opposite effect has been noted for B doping, where smaller dot sizes have been reported. The reason for this is presently unclear, but a tentative explanation of this effect might be that local deformation induced by impurity atoms suppresses QDs formation. It is however possible to introduce doping atoms by post-annealing diffusion, with no effect on the crystals size [29]. It has been demonstrated that it is possible to obtain rectifying junction combining p- and n-type doped nanostructured films. This proves that some sort of doping is really taking place in the films [30] [31] [32]. It is, at present, unclear what the mechanism of doping in these structures is, but some general remarks can be made. A 'bulk-like' doping mechanism is the easiest model that can be analyzed. For this to happen it is necessary that at least one atom of the dopant is incorporated in the nanocrystal during its growth. It is unclear if this can happen as theoretical calculations have shown that the impurities will tend to be expelled by the perfect small nanocrystals and segregate at the interface. In [33] a doped-QD is treated as a Si sphere with B or P (for p- and n-type doping respectively) in substitutional position. A simulation is then run varying the dimension of the aggregate. The formation energy of the impurities is defined as the energy required to insert an atom X with chemical potential μ_X inside a cluster of n Si atoms and m H atoms to terminate dangling bonds ($\mathrm{Si}_n\mathrm{H}_m$) after the removal of a Si atom:

$$E_f = E(Si_{n-1}XH_m) - E(Si_nH_m) + \mu_{Si} - \mu_X \tag{2.8}$$

This is showed to be higher in the QD then in the bulk being a decreasing function of the size of the cluster (Fig. 2.5) leading to more

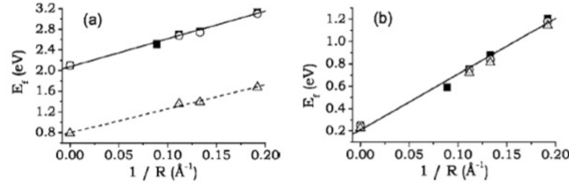

Figure 2.5: Formation energy of neutral impurities at the center of a Si-QD as a function of inverse radius for B atoms (left) and P atoms (right). Inverse radius equal to zero is the bulk value.

stable structures with increasing size. This impurity also induces a change in the structural properties of the cluster. Around the impurity a reconstruction takes place where the B atom is shifted toward the $\langle 111 \rangle$ direction that affect the Si-B bond length. This is the first hint that a segregation might take place. The study of the formation energy as a function of the position of the substitutional atom (Fig. 2.6) shows that, as long as the atom is in the core of the nanocrystal, the formation energy is almost constant (path $1 \rightarrow 2 \rightarrow 3$). If the impurity is moved to the interface, than the formation energy drastically decrease (paths $3 \rightarrow 4$ and $5' \rightarrow 6'$). This is explained by the fact that this position is the only one allowing a relaxation of the atoms around the impurity. According to a very recent paper [34] it is only possible to dope a QD with a very high concentration of dopant after all the sites at the interface have been filled with the impurities.

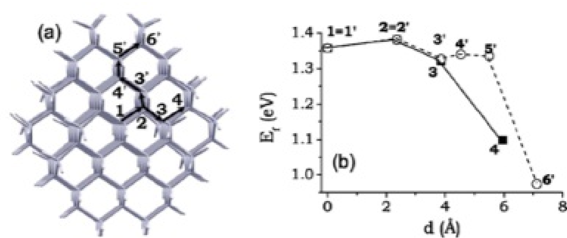

Figure 2.6: Formation energy of neutral impurities as a function of impurity position in the QD.

Chapter 3

Samples description

In this thesis work several SRO samples have been analysed, each one designed for a particular characterization technique. These samples come from Fondazione Bruno Kessler (FBK) in Trento whose growth technique is PE-CVD and University of New South Wales (UNSW) in Sydney, grown by co-sputtering. All of them have been grown on $\langle 100 \rangle$ c-Si wafer $525 \mu m$ thick or on quartz if lateral electrical measurements are needed.

3.1 Single layer thick films

The first set of sample that will described are the ones received from FBK for electrical as well as optical measurements. These samples are deposited on $\langle 100 \rangle$ $10\ \Omega \cdot cm$ p-type silicon wafer to allow for Fourier Transform-Infrared (FTIR) spectroscopy and for vertical geometry electrical measurements. They are provided with a metal mask (Fig. 3.1) with different contact geometries to allow for the measurements of different transport mechanisms. There are two wafers for each stoichiometry determined by the 'Γ' parameter: $\Gamma = \frac{flux(N_2O)}{flux(SiH_4)}$.

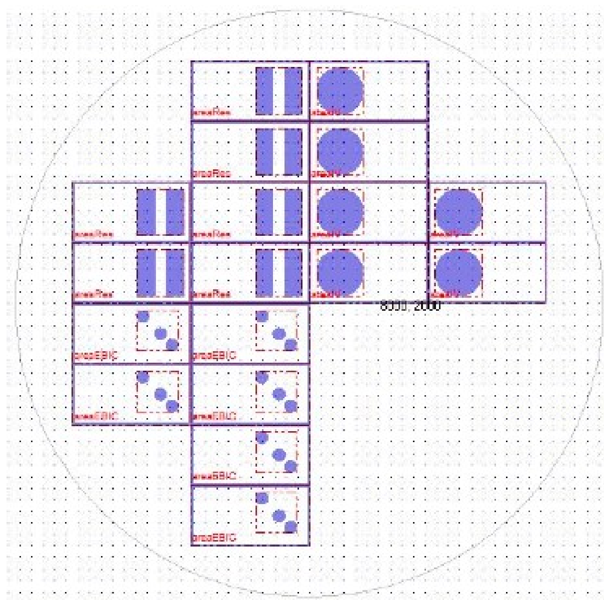

Figure 3.1: Layout of the metal mask used to deposit electrical contacts.

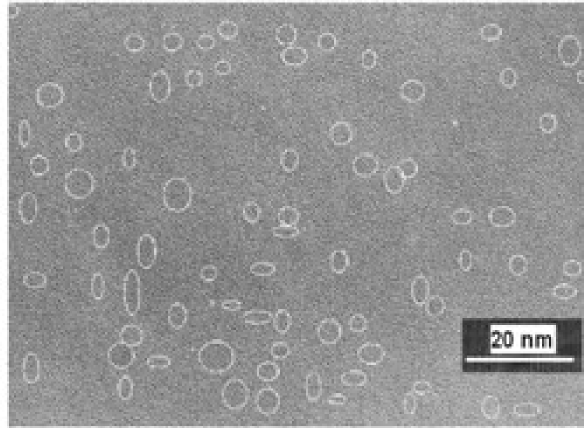

Figure 3.2: TEM image of a sample analogous to the one described in this section.

This growth parameter represents the ratio of the fluxes of two gases used for the deposition: the nitrous oxide (which is the oxygen source) and the silane (the silicon source). The higher the Γ the lower the silicon content and hence the more stoichiometric the layer.

For every stoichiometry, one wafer is then annealed to form the nanocrystals (Fig. 3.2) or left as deposited to act as a 'blank' sample for comparison. After the deposition and the possible annealing, the metal contact on the front are deposited with a mixture of Al and 1% Si $1\mu m$ thick to prevent spiking (Fig. 3.3).

The thickness of the films was measured both as the result of the calibration of the CVD apparatus in term of deposition rate and total deposition time, and with spectroscopic ellipsometry, that also provides the refractive index. Both these values are in agreement with the expected trend of decrease in thickness and increase in refractive index after the annealing, with bigger differences for the samples with

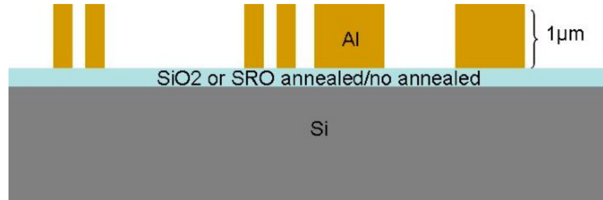

Figure 3.3: Schematics of the sample section.

higher silicon excess, with no differences for stoichiometric silicon dioxide. This is expected because the annealing drives hydrogen out the samples and let the silicon in excess segregate, so that the films shrinks while keeping the mass constant. This increase the density and hence the overall refractive index.

A summary of the samples can be found in Tab. 3.1.

3.2 B-doped multi-layered films

Another set of samples analysed with optical and electrical techniques was prepared via sputtering deposition by the University of New South Wales using a computer-controlled AJA ATC-2200 sputtering system. They were deposited on double-sided polished high resistivity intrinsic floating zone silicon. The samples were boron-doped and were analyzed looking for the boron ionization level (provided that the impurities were being included as dopant inside the nanocrystals). For this reason the samples were multi-layered with different dot size and different amount of dopant. The control of the amount of B atoms in each layer was achieved by varying the power applied to the boron sputtering target (see Tab. 3.2). All the samples were further annealed at 1050℃ to form QDs.

The first set of samples (from JM8 to JM13) was the first one

Table 3.1: Description of the thick mono-layered samples.

sample	material	annealing @ 1050℃	thickness (nm)	refractive index @ 630nm
SRO1	SiO_2	no	69	1.493
SRO2	SiO_2	yes	69	1.494
SRO3	SRO Γ3	no	77	2.078
SRO4	SRO Γ3	yes	53	2.563
SRO5	SRO Γ10	no	73	1.717
SRO6	SRO Γ10	yes	62	1.882
SRO7	SRO Γ15	no	64	1.621
SRO8	SRO Γ15	yes	62	1.742

received, but a contamination in the furnace used for the annealing (probably a cross-contamination from the samples), made the identification of boron less conclusive (see section 4.3) prompting the need to have another set of samples from another batch. The thickness of the samples was measured by knowing the deposition rate (via a calibrated deposition monitor, built in in the sputtering) and the total deposition time. In the second batch of the samples two 20 nm SiO_2 diffusion barriers were deposited directly on top of the Si wafer (to prevent B out-diffusion) and on top of the film, while in the first one only the capping layer is present, to prevent damages.

Table 3.2: Description of the multi-layered samples. The horizontalline divides the samples coming from the two annealing batches as explained in the text

sample	bi-layer n°	SRO thickness (nm)	SiO_2 thickness (nm)	B target power(W)
JM8	25	4	2	20
JM9	25	5	2	20
JM10	25	4	2	30
JM11	25	4	2	0
JM12	1	0	96	20
JM13	1	0	96	0
JM14	25	4	2.5	0
JM15	25	4	2.5	20
JM16	25	5	2.5	20
JM17	25	0	5+2.5	20
JM18	1	0	100	0

Table 3.3: Description of the multi-layered samples for electrical measurements.

sample	bi-layer n°	SRO thickness (nm)	SiO_2 thickness (nm)	Γ
MIL15	10	1.5	1.5	3
MIL30	10	3	1.5	3

3.3 Multi-layered films for electrical measurements

The set of samples specifically designed for electrical measurement was received from FBK. This set served as a comparison between the transport in 'bulk' material and in multi-layered one. It uses the same contact mask as the one depicted in fig 3.1 and the two different wafers are of the same stoichiometry, the $\Gamma = 3$. The difference of the two wafers lies in the thickness of the SRO layer (and hence of the QDs), as visible in Tab. 3.3.

All the samples have been annealed at 1050°C for one hour to nucleate the dots.

3.4 Samples for stoichiometry assessment

This set of samples, grown in UNSW by co-sputtering, has been used for the development of a novel technique to assess the stoichiometry of SRO-SRN films. Each film has been deposited on both silicon and quartz to allow for IR spectroscopy (the ones on silicon) and UV-VIS spectroscopy in both reflectance and transmittance (the ones on quartz). They are all single-layered, with the deposition of SiO_2 occurring at the same time as the Si one. The different silicon excesses

Table 3.4: Description of the samples for stoichiometry assessment.

sample	Si sputter target power (100%=300W)	thickness (nm)	n(@ 680 nm)
A	20%	221.3	1.70
B	35%	274.9	2.20
C	50%	257.7	2.56
D	65%	244.2	2.87

in each sample has been obtained varying the power applied to the silicon target and hence its sputtering rate.

The samples have been characterized with different optical techniques. The thicknesses have been determined by X-Ray Reflectance, the visible reflectance and transmission with an UV-VIS spectrophotometer and the IR absorbance with an FTIR device. Half of each samples deposited on quartz has been annealed by rapid thermal annealing and patterned or lateral electrical measurements.

The summary of the samples are in Tab.3.4

Chapter 4

Optical characterization by IR spectroscopy

4.1 Theory

Infrared spectroscopy is a powerful spectroscopic technique that can be used to asses the chemical composition of a substance. It is based on the fact that IR photons have an energy that correspond to a range of energy where chemical bonds in the molecules can vibrate and thus can absorb photons that resonate at a particular energy characteristic of the bond and the chemical environment. In particular, the range of wavenumber used for our instrument (400-4000 cm^{-1} corresponds to the typical range of the roto-vibrational modes of vibration of the molecules. This techniques takes advantage of the comparison between the absorption spectrum of a sample and the same spectrum of a reference experimental condition such as the empty chamber (so that the residual spectrum corresponds to the sample and the substrate absorption) or, even better, the substrate itself (so that the residual spectrum corresponds to the film deposited on the surface). This

subtraction is usually very precise and can detect doses or elements (the quantity per unit area) of down to $\simeq 10^{13}\mathrm{cm}^{-2}$ depending on the strength of the bond.

The mathematical treatment of the data stems from the Lambert-Beer's law which states that the intensity I of a radiation beam of intensity I_0 that undergoes absorption traveling through a slice of material whose thickness is l that has C moles per unit of volume and ϵ molar absorptivity is:

$$I(E) = I_0(E)10^{-\epsilon(E)\cdot C\cdot l} \tag{4.1}$$

It is clear that, taking the ratio $\frac{I(E)}{I_0(E)}$ it is possible to evaluate the transmission coefficient $T(E)$ which is the probability of a photon of energy E to be absorbed. By taking the base-10 logarithm of the inverse of this quantity, one gets the absorbance:

$$ABS(E) = \frac{1}{\log(T(E))} = \epsilon(E)\cdot C\cdot l \tag{4.2}$$

which is proportional to the thickness of the sample, making two different absorbances directly comparable by just dividing them for the respective thickness.

Of course this value is only a first approximation of the complicate process of light travelling in a medium, since it ignores:

- the cross talk between absorbers
- the scattering of the light in the medium
- the different optical path of a IR beam which is not collimated
- any inhomogeneity of the absorbing medium
- the influence of the beam (i.e. heat released in the medium) that might change the optical and absorption properties of the medium

Since these effects are usually small enough for our samples, we will neglect them and assume equations 4.1 and 4.2 to be a good approximation.

4.2 Stoichiometry assessment

From Eq. 4.2 it is possible to derive that IR spectroscopy might be used to measure the thickness of a sample of known composition either by obtain a calibration sample of known thickness and measuring its absorbance, or by knowing the $\epsilon(E)$ and calculating it from the start. It must be emphasized that the area under the desired peak must be used to correctly calculate the absorption of a bond because there are several effects that blurs the absorption.

Using the first method, it is possible to obtain a calibration curve of the absorption of a film of silicon dioxide. We prepared a set of sample of silicon dioxide on c-Si by performing a dry oxidation at 1000°C in O_2 of a regular, double-polished silicon wafer. To measure the thickness, ellipsometry can be safely used. By performing successive etchings in a solution of buffered HF and by measuring, after each step, the thickness of the residual oxide and the relative absorbance, it is possible to draw a calibration curve of the thickness versus the integral area under the peak at 1080cm^{-1} that corresponds to the asymmetric stretching mode of the Si-O bond. From fig. 4.1 it is clear that the linearity is very precise and hence this method can be safely used as an alternative way of determining the thickness of a SiO_2 sample. The same technique can be used to asses the thickness of a nitride sample.

This procedure has been used for two different purposes: the calibration of a solution of HF that allows the removal of the capping layers of the samples without etching the films and the calculation of the stoichiometry of the samples.

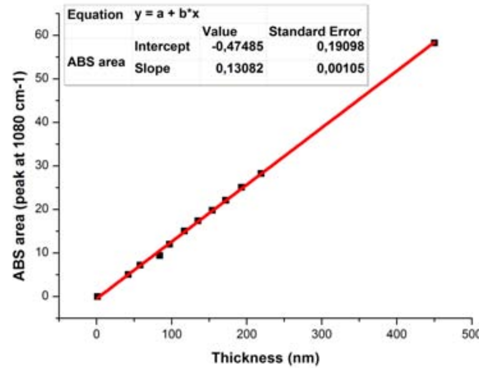

Figure 4.1: Thickness calibration curve.

For the preparation of a HF solution, it has been exploited the fact that the etch rate of the solution is strongly dependent on the stoichiometry, being much higher in silicon dioxide than in SRO. By measuring the thickness of a thermal silicon dioxide sample before and after the etching procedure and by timing the etching, it is possible to derive the etch rate of the solution used, as can be seen in Fig. 4.2. By changing the dilution of HF, the etch rate changes accordingly. We used for the most part a solution of HF 1%vol. because it provides an etch rate of around 0.6nm/s which is neither too low that it takes a long time to perform, nor too fast that the film under the capping layer risks to be damaged.

For the assessment of the stoichiometry we deposited four SRO films with different silicon composition, on both, 1 mm thick quartz substrates and, on ⟨100⟩, 525μm thick, p-type (1-10 Ωcm resistivity) silicon substrates. The samples deposited on quartz have been annealed by rapid thermal annealing and used for UV-VIS transmittance

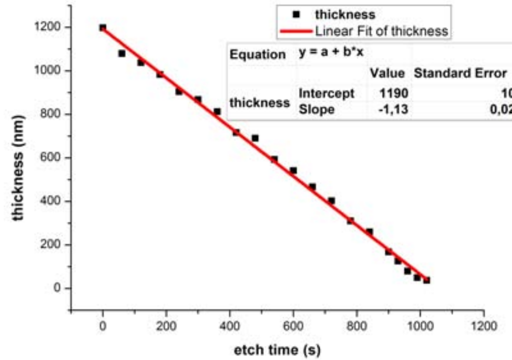

Figure 4.2: Calculation of the etch rate of a solution 1% vol.

measurements while those on silicon were left as deposited and used for FTIR spectra acquisition. The deposition was performed using a computer-controlled AJA ATC-2200 sputtering system. The stoichiometry of the film was varied from sample to sample by increasing the power applied to the silicon target, while keeping constant the one of the silicon dioxide target. The assumption is that the silicon excess in the film is directly proportional to the power on the silicon target above the deposition activation threshold in the range considered. The samples have been measured with a NICOLET 5700 FT-IR from Thermo under dry N_2 purging. The absorbance spectrum is obtained from the sample by measuring the spectrum of the substrate suitably kept from any process and comparing it to the spectrum of the sample with the film deposited on the front surface. The final spectrum is the result of 100 averages of a single spectrum. PANanalytical X'Pert MRD was configured for X-Ray Reflectivity (XRR) to examine the SRO layer thickness. The primary X-Ray source is CuKα

(λ=0.154 nm), which is defined by divergence slit of 1/4°(divergence of 0.27°). Soller slits with 2.3° divergence were installed for incident and reflected beams. A 1/32° anti-scatter slit was used to improve resolution. A PIXcel3D detector was used and configured in 'receiving slit' mode to give better signal counts. For better statistical data, slow scanning speed and low scanning step were used to scan over the 20x15 mm^2 sample area. The software X'Pert reflectivity was applied to calculate the thickness of the SRO. The Fourier method involving automatic Fourier volume calculation was used to show clear peak values to identify the thickness, which eliminated errors from manually reading neighboring fringe peaks. The transmission of Silicon Rich Oxide thin films on quartz substrate was measured using a UV/VIS Lambda1050 PerkinElmer spectrophotometer. A wavelength range from 200 to 2500 nm in 2 nm increments was used at an incident angle of 0°. Two detectors were used for the transmittance measurement, a Photomultiplier Tube (PMT) was utilized for 200 nm to 860 nm and an InGaAs photodiode detector for 860 nm to 2500 nm. To qualitatively evaluate optical and compositional properties of SRO, the WVASE simulation software tool from J. A. Woollam Co. was used to simulate the transmittance results using a Bruggeman Effective Medium Approximation (EMA) model.

We gathered all the FT-IR absorbance spectra of the films, taken with respect to the substrate. The area under the Si-O asymmetric stretching vibration mode around 1080 cm^{-1} has been calculated from each spectrum, using a suitable baseline and spanning the same range from 800 cm^{-1} to 1300 cm^{-1} (Fig. 4.3) and normalized for the film thickness. Within EMA model, it is possible to describe a film of SRO of generic stoichiometry by:

$$SiO_x = \alpha Si + \beta SiO_2 \tag{4.3}$$

Hence:

$$x = \frac{\alpha + \beta}{2\beta} \tag{4.4}$$

The case $x = 0.5$ is the stoichiometric silicon dioxide, while for SRO $x > 0.5$. In our case the XRR measurements fixed independently the thickness values. The basic idea of our model is the a generic SRO film can be thought as composed of two layers, one of stoichiometric silicon dioxide of thickness t_{SiO_2} and the other of silicon, with thickness t_{Si}. the relationship between the two is:

$$t_{SiO_2} = \chi \cdot t_{SRO} \tag{4.5}$$

$$t_{Si} = (1 - \chi) \cdot t_{SRO} \tag{4.6}$$

where χ is the ratio of the density of Si−O bond in SRO and SiO_2, respectively C_{SRO} and C_{SiO_2}. By applying the definition of absorbance, it is possible to relate the Cs to the area of the peak at 1080cm^{-1} normalized to the thickness as follows:

$$\chi = \frac{C_{SRO}}{C_{SiO_2}} = \frac{A_{SRO}}{t_{SRO}} \cdot \frac{t_{SiO_2}}{A_{SiO_2}} \tag{4.7}$$

If the effective medium approximation was strictly valid, the area under the band for a given film thickness should decrease linearly with the silicon richness, since less Si−O bonds are present, replaced with Si−Si bonds. With some manipulation, we can obtain the stoichiometry x in terms of quantities that we know or we can measure with the IR:

$$x = \frac{1}{2} + \frac{(1 - \chi)}{\chi} \frac{C_{Si}}{C_{SiO_2}} \tag{4.8}$$

where the values for the stoichiometric silicon dioxide must be measured on a reference sample and $C_{Si} = 2.27 \cdot 10^{22} cm^{-3}$ and $C_{SiO_2} = 5 \cdot 10^{22} cm^{-3}$ are the tabulated bond densities for, respectively, Si−Si bond in c-Si and Si−O bonds in SiO_2. From the data is possible to see

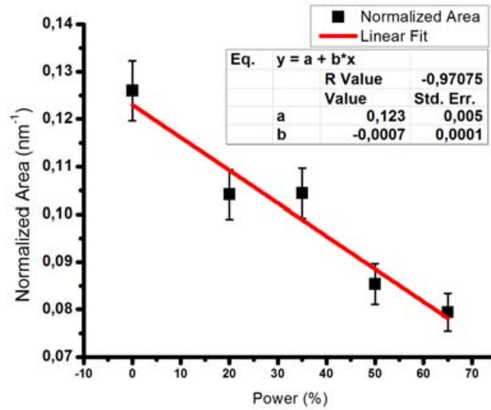

Figure 4.3: Calculation of the stoichiometry from FTIR measurements.

a trend where the normalized areas decrease as the silicon content increases. The linearity is followed also if we add to the graph the point corresponding to the normalized absorption area of a stoichiometric silicon dioxide sample (obtained setting to 0% the power applied to the silicon target), as can be seen in Fig. 4.3.

The uncertainties inherent to this method are to be ascribed to the difficulty in setting the correct baseline and range of integration for each spectra, in particular with single side polished wafers. Also the error in the thickness plays a minor role in the determination of the precision of this method. Our estimate for the total error is roughly 5% of the value, which is accounted for in the error bars shown in Fig. 4.3. We simulated the transmittance of Silicon Rich Oxide thin films using Bruggemann effective medium approximation (EMA) [35]. Although the Tauc-Lorentz model [36] is widely used for modelling amorphous dielectric materials with absorption and, by selecting the proper oscil-

lators [37], to closely reproduce the measured transmittance of these films, it does not address the composition of mixed constituent films. We used an EMA model to represent the mix of SiO_2 and c-Si and utilized this method to evaluate the concentrations of Si corresponding to increasing Si sputtering power when depositing these films. The use of c-Si rather than amorphous Si as the more appropriate choice is due to the rapid thermal annealing process at 1100℃ after deposition, which should induce silicon crystallization. The superior fitting results also support the use of c-Si as a more acceptable choice. The thickness was fixed according to XRR results to reduce fitting parameters, so only the SiO_2 and c-Si volume fractions need to be fitted. Since an increased Si concentration enhances the absorption of SRO film in a manner not yet understood, the absorption wavelength region from 220 nm to 1000 nm was not fitted. Instead, the non-absorbing region of the spectrum extending from 1000 to 2500 nm was the spectrum used for the data fitting (see Fig. 4.4). In this region of the spectrum, Si and SiO_2 are transparent materials. As a result, only the real part of the refractive index 'n' needs to be taken into consideration and the extinction coefficient 'k' can be ignored. The structure used in our model contained an EMA SRO layer of variable thickness and a 1mm thick SiO_2 substrate. No intermix layer or surface roughness was added for these were not required to obtain good fittings. The fitting results are listed in Table 4.1 including thickness, composition and the Mean Squared Error (MSE). Refractive index is also included in the table, which increases with increasing silicon richness.

It can be seen from the table that the simulated increasing silicon richness result is consistent with the increasing sputtering power on the silicon target. MSE values less than one indicate good fitting results that arise also because we reduced the number of free parameters by measuring the thickness independently. The uncertainties in the thickness and the fitting procedure combined introduce roughly a 3% error in the calculation of the Silicon content which is reflected in the

Table 4.1: Summary of the measurements of the samples for stoichiometry assessment.

Sample	Si target power (100%=300W)	thickness (nm)	n @ 680 nm	SiO_2 (%)	Si (%)	MSE	Normalized Area (nm^{-1})
A	20%	221.3	1.70	86.11	14.3	0.39	0.1042
B	35%	274.9	2.20	54.01	35.01	0.65	0.1044
C	50%	257.7	2.56	51.82	49.1	0.89	0.0854
D	65%	244.2	2.87	41.02	59.7	0.54	0.0794

error bars in Fig. 4.4. As can be seen, the fit depicted in Fig. 4.4 is consistent and can be used as a first guess to give a semi-quantitative estimate of the SRO Si composition by plotting the results from the fit of the absorbance in the UV-VIS range versus the normalized area derived from the IR measurements (Fig. 4.5). This graph provides us with the link between integral area of the absorption peak of the Si−O asymmetric stretching mode and the silicon excess in a film of SRO. Using it we can assess the SRO composition by a quick, non destructive IR measurement of the absorbance of the film. We can observe, however, that sample B is off the calibration curve. It should be noted that this sample also show the least agreement with each method, suggesting incorrect handling during the deposition or during the thickness measurement. Investigations on this sample are being carried out. Finally, a sample with known composition (via, i.e., Rutherford Back Scattering technique) is under preparation and will eventually provide a calibration for this method [38], allowing its use for the assessment of the absolute stoichiometry of such films.

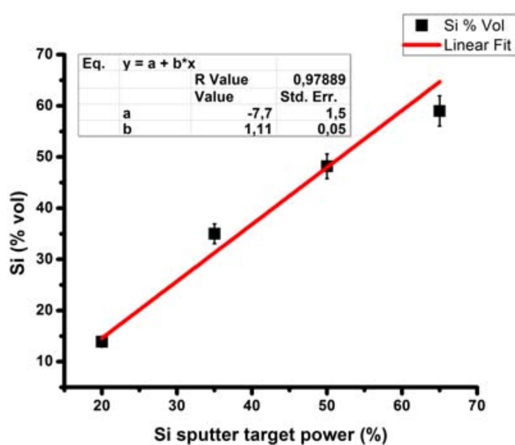

Figure 4.4: Calculation of the stoichiometry by UV-VIS measurements.

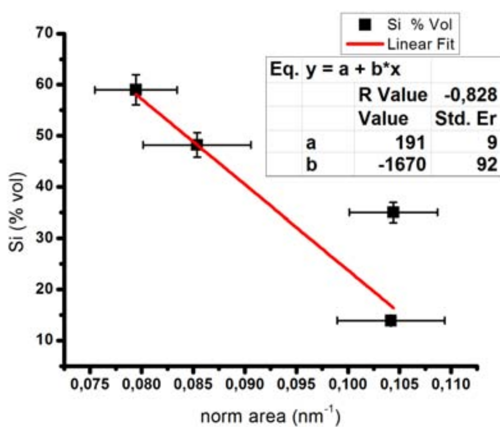

Figure 4.5: Correlation between UV-VIS and FTIR measurements.

4.3 Identification of B-levels

The binding energy E_B of a donor is defined as the difference between the lowest conduction band state of a nanocrystal with an excess electron with and without the impurity atom. Such values are calculate in [39] as a function of the dot diameter. The expression the authors extract is:

$$E_B(R) = \left(\frac{1}{\epsilon_{out}} + \frac{1.44}{\epsilon_{in}}\right)\frac{e^2}{R} \tag{4.9}$$

where ϵ_{out} is the dielectric constant of the matrix embedding the QDs, ϵ_{in} is the dielectric constant of the 'bulk' material of the nanocrystals, e is the elementary charge and R is the size of the crystal. In the bulk this is the ionization energy since the conduction band is continuous, while in the nanocrystal immersed in a dielectric matrix, to calculate the ionization energy, at the binding energy must be added the potential barrier between the dot and the conduction band of the matrix.

Here the table of the samples used for the identification of B levels is presented again in Tab. 4.2. In the first set of samples (from JM8 to JM13) we were able to identify B electron levels in Si as can be seen in Fig. 4.6. These spectra were taken at low temperature ($\simeq$30K) in the spectral range 400-50cm$^{/1}$. According to ASTM, these peaks can be safely attributed, as said, at electronic levels of B in Si. A careful consideration of the spectra, however, shows that it is possible to detect boron signal also in samples with no boron in it, namely JM11, as can be see in the following Fig. 4.7 With this evidence, we ascribed this signal to contamination of the substrate by boron cross contamination during the annealing step of the preparation, explanation that is backed up by our measurements of the sheet resistance of the substrate backside performed by four point probe. We focused then on the other set of samples deposited with some precautions, such as the annealing of JM14 and JM18 during another batch.

Table 4.2: Description of the multi-layered samples.

sample	bi-layer n°	SRO thickness (nm)	SiO_2 thickness (nm)	B target power(W)
JM8	25	4	2	20
JM9	25	5	2	20
JM10	25	4	2	30
JM11	25	4	2	0
JM12	1	0	96	20
JM13	1	0	96	0
JM14	25	4	2.5	0
JM15	25	4	2.5	20
JM16	25	5	2.5	20
JM17	25	0	5+2.5	20
JM18	1	0	100	0

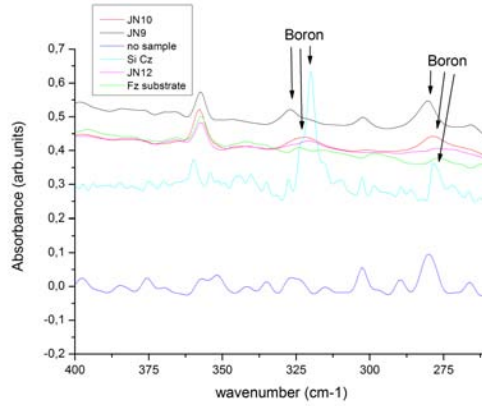

Figure 4.6: Spectra of samples JM8-JM13. The peaks ascribed to boron are marked with arrows.

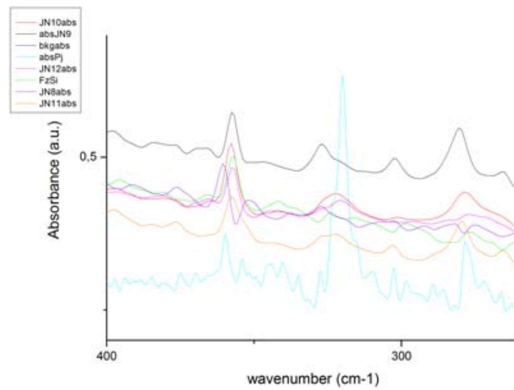

Figure 4.7: Spectra of samples JM8-JM13. In JM11 the peaks of boron are also visible.

Our FTIR system can perform measurements at low temperature, but since the energy of the bonds are such that the cannot be ionized at room temperature (being them at $\simeq 10k_BT$), we performed all the measurements at 300K. The spectral range of our measurements was $400-4000cm^{-1}$ with a resolution of 4 or $2cm^{-1}$. This range is suitable since the B-O bonds lies in a band around $1350-1400cm^{-1}$ and that the B ionization energy in a 4nm Si QD in a SiO_2 matrix should be around $2200cm^{-1}$. All the measurements were performed in vacuum to reduce the contribution of inconstant residual CO_2 and H_2O in the chamber. Those molecules have the stretching bands of their bonds at, respectively, $2300-2350cm^{-1}$ and $1300-1400cm^{-1}$ and their intensity would be far higher then the ones we are interested in.We gathered all the spectra of absorbance versus the empty chamber for all the samples and compared them. For each spectrum we collected the maximum allowed number of scans (32000) to improve the signal to noise ratio.

The first striking difference is in the peaks around $1080cm^{-1}$ of samples JM14,15 and 16 with respect to samples JM17 and 18. The latter shows a relatively simple peak at $1080cm-1$ while the former shows a more complex band around this value. This is typical and due to the non-stoichiometry of the film as explained before.

By comparing the spectra of JM14 and JM15 in the region of interest, there are no remarkable differences that can be ascribed to the presence of boron as dopant or as IR-active inclusion in the film. Even after different experimental setup (such as directly measuring the absorbance of the film with respect to the substrate or using JM14 as the background for the JM15), no evidences of the presence of boron were detectable. The possible explanations for this observation are three. The first one is that the B atoms are expelled from the perfect nanocrystal and segregate either at the interface between the dot and the matrix or directly in the matrix where it cannot act as substitutional impurity and form either B-B bonds or B-O bonds. An explanation of the impossibility to detect these bonds is that the dose

of the atoms are so low that they are under the threshold. The second reason that might prevent us to detect the levels is that these levels are dependent on the size of the dots. Since the dose of the dots is, in our case, $10^{12}/cm^2$, which is already very close to the detection limits of transmission FTIR, if the dots are not close to be monodispersed, the spectrum will be so broad that the signal will not be detectable. The third explanation is that the B atoms are acting as dopants but the signal at $2200cm^{-1}$ is not detectable because the levels are already self-ionized because of the confinement as suggested in Ref. [40]. In this case the IR photons would not be absorbed because the levels towards which the electrons are making the transition would already be full. To address this issue we performed measurements by shining white light from 4 LEDs over the sample to try and promote some electrical transitions and freeing otherwise frozen levels. Also in this case no evidences of transitions around $2200cm^{-1}$ are detectable.

The first two explanations of this behavior still hold, but to gain further insight, also considering [34], we are planning to perform measurements in a different geometry (attenuated total reflection in multiple internal reflection - ATR-MIR). These measurements require the films to be deposited on a double-polished silicon prism that will act as the optical element through which the IR beam will propagate. By employing a suitable geometry of the entrance window, the beam will be reflected inside the prism itself at an angle greater than the critical angle between the silicon and the film and hence it will be fully reflected multiple times, hence the multiple internal reflections. A part of the beam, however, will propagate into the film as the so called 'evanescent wave' and will be missing from the reference sample. Depending on the number of the internal reflections (which is essentially a geometric property of the optical system and the prism) the missing signal will be attenuated more and more, making it possible to increase the apparent optical path travelled through the medium and hence the value of the absorbance. Our system features 110 internal

reflections (220 if the film is deposited on both the faces of the prism) and hence the signal strength can be increased by more than two orders of magnitudes making it possible, maybe, to detect these faint signals.

Chapter 5

Electrical transport in nanostructured Silicon dioxide films

A large part of my work has been devoted to give a better insight to the electrical transport mechanism that take place in films suitable for advanced photovoltaic use. Since the films usually used for these purposes are made of a large dielectric part, charges usually travel through these films with difficulty, unless the deposition parameters and nanostructuration are carefully optimized. The understanding of the transport is therefore crucial.

5.1 Experimental setup

The measurements on dielectric films such as (in principle) the samples studied for this thesis, require the ability to detect small currents due to the very high resistances typically encountered in insulators. It is also necessary to be able to vary the temperature of the sample to

probe the possible change in transport process and activation energy with the temperature. For this purposes we used two different experimental setup one for the low temperature regime and the other for high temperature. We performed also a set of measurements at room temperature and at high applied voltages.

5.1.1 Samples preparation

Before describing the experimental setup for each measurements performed, the general sample preparation procedure will be described.

Each samples is shipped featuring a capping layer of SiO_2 that has to be removed in order to study the electrical transport in the active layer without this unneeded series resistance. For this purpose, we cleaned the surface of the sample with a Piranha solution (a mixture of 3 parts of H_2SO_4 with 1 part of H_2O_2) to remove all the organic contaminants. Then, as described in Section 4.2, we prepared (after some calibration tests), a solution of HF 0.5% vol. for a period of time appropriate with the thickness of the capping layer, keeping in mind that the etch rate of that solution is around 05 nm/s. After this step, if the samples where already metallized with a contact of an alloy made of Si and 1% Al, we proceeded to perform the measurements. If not we evaporated Al using a shadow mask to define the contact area and then covered this layer with a film of sputtered gold in order to prevent contact oxidation. In both cases the back contact was made scratching with a diamond tip an eutectic mixture of In and Ga the back surface of the substrate. This alloy is liquid at room temperature and make a good ohmic contact with p-type Si, also providing some mechanical adhesion to the base. To improve the adhesion and to enhance the thermal contact, we also used silver paint on the back of the sample.

5.1.2 Low temperature setup

For the low temperature region, we adapted an Hall Effect measurements system to act as measuring device. A Keithley 617 electrometer with a minimum detectable current of 1nA was used in source-meter configuration. It apply a constant voltage in the range ±5V with the positive terminal being connected to the p-type substrate and the negative terminal (connected to the front contact of the sample) grounded. If a more extended voltage range was needed, the full apparatus was used. It features the same Keithley 617, this time used as electrometer, a Keithely 181 as voltmeter, a Keithley 220 as the current source.

The low-temperature regime was achieved with an Oxford Instrument Cryostat controlled by a Leybold LTC-60 low temperature controller. The cryostat features a two stages liquid He pump that can reach a temperature of the cold finger down to T≃10K. The controller feature a PID controlled heater that can rise the sample temperature. The stability of the sample temperature was reached in just a few minutes. This temperature was measured using a Si-diode thermometer from Scientific Instruments which feature a 0.1K precision.

A good thermal contact with the cold finger is required if the sample has to reach the lowest possible temperature,. It is, however, needed that the sample is electrically insulated from the cold finger since this is grounded by the cryostat. To do so we employed a very thin ($\simeq 50\mu m$) flake of mica or sheet of Mylar. This ensures a good electrical insulation, but allow the sample to reach temperatures only as low as ≃30K (as determined putting a Si-diode thermometer in the same position as the sample) but that are enough for our purposes. The sample is attached to the Mylar sheet using silver paint that feature the best possible thermal contact.

The contacts between the metal and the measurement system have been done using copper wire glued to the metal with silver paint. This has the advantage of being easy to do and of being tolerant to the

shrinking due to the low temperature, but the downside is that after one measurement is performed, one has to prepare the contact again or the behaviour of this part of the system is not exactly reproducible. For some measurements we used, instead, a tungsten tip with a spring loaded to touch the metallization, with a drop of silver paint on it to avoid scratching directly the film. This system has proven more reliable and easier and hence has been used since its implementation afterwards.

All the measurements, also the ones at high temperatures, have been performed in vacuum (to avoid condensing of water and oxidation of the metals) and starting from the lowest temperature and rising, as to allow for better thermalization of the samples.

5.1.3 High temperature setup

The system for low temperature cannot be used for temperature higher than $\simeq$ 320K because of a limitation in the output power of the heater. For this reason, another cryostat (Microstat^{He}) from Oxford Instruments and its controller have been used together with the Keithley 617 mentioned before in source-meter configuration. For this purpose we developed a set of copper bases with plugs for the contacts and a tungsten, spring-loaded tip that could be placed over the contacts to allow for an easy loading of the sample in the cryostat (Fig. 5.1).

The connections to the vacuum feedthrough were made with copper wires. The choice of copper for the bases was due to its very high thermal and electrical conductivity because each base serves as back contact for our measurements and as thermal reservoir to keep the temperature as stable as possible. As before, to insulate the base from the cold/hot finger of the cryostat, we used a Mylar sheet or a mica flake. The temperature was monitored with the built in thermometer of the controller and serves also as feedback signal for the PID. The Mylar sheet was glued to the finger of the cryostat and the base to the

Figure 5.1: Picture of the sample holder. In this figure the tungsten tip and the electrical connections are clearly visible.

other side of the sheet via Apiezon vacuum grease which also increases and the enhances the thermal contact between the components.

This cryostat features a quartz window directly on top of the position where the sample is when it is mounted on the cold finger. This windows makes it possible to shine light on the sample while performing IV scans. We took advantage of this possibility to measure the photoresponse of a set of samples that has been described earlier. For the illumination we used a 150 W white halogen lamp coupled with an optical fiber system that we kept normally to the surface of the window and as close as possible for the reliability of the measure. We obscured the window when working in dark to minimize the effect of stray light.

5.1.4 High voltage setup

For one set of samples we performed measurements with high polarization and current. The measurements could no be carried out with the Keithley 617 source-meter because it has a maximum tension output of ±5V and compliance current of 2mA. To overcome this limits, we used instead the Keithley 2420 which features a voltage range of ±48V with a 3A compliance current. The remeaining setup is the same as the one for high temperature measurements.

5.2 Transport in films with different SRO stoichiometry

The transport in SRO films, nanostructured or not, is assumed to be stoichiometry dependant. This means that each different stoichiometry will have a different transport mechanism or at least will show a different mean resistivity. It is not granted that the more the silicon richness the lower the resistance, but there will be most likely an optimum stoichiometry that will have the lowest resistance. This observation does not have to be mistaken with the optical absorption that depends as well on the stoichiometry. The tuning of the absorption is due to the presence of a well ordered array of quantum dots and by their dimension. This last parameter depends only on the thickness of the SRO layer and not by the stoichiometry, while the density of the QDs will depend on the excess silicon able to coalesce in nanocrystals.

The samples used to assess the effect of the stoichiometry on the resistivity are the ones used for the IR measurements to asses their composition. They are summarized in Tab. 5.1.

The samples have been annealed by rapid thermal annealing at 1000°C to nucleate QDs and a layer of aluminium has been deposited on them with a lithographic mask. This pattern has some features on

Table 5.1: Description of the samples for IV measurements with different stoichiometries.

sample	Si sputter target power (100%=300W)	thickness (nm)
A	20%	221.3
B	35%	274.9
C	50%	257.7
D	65%	244.2

it that allow the measurements of the resistivity of the film correcting for the contact resistance. This method is called Transfer Length Measurement (TLM). This method has been proposed by Shockley and described in [41]. In general a TLM test is performed using a two terminal contact test structure, consisting of more than three pairs of contacts each one featuring a different spacing. From this linear TLM structure the contact resistance and specific contact resistance can be determined through the linear relationship between the resistance and the gap spacing the contacts. The linear TLM technique, however, tends to suffer from the fact that currents from one contact to another contact may spread due to current crowding [42]. To overcome this problem, circular TLM (cTLM) has been proposed. This method consist on a series of metal circles surrounded by a metal contact leaving a space of semiconductor between the two metallizations (Fig. 5.2. The linear relationship between the gap and the resistance does not hold any more, replaced by a logarithmic dependence, but in this way no current crowding can happen. By plotting the resistance measured versus the natural logarithm of the ratio of the two radius (inner and outer), the sheet resistance is proportional to the slope of the curve obtained [43].

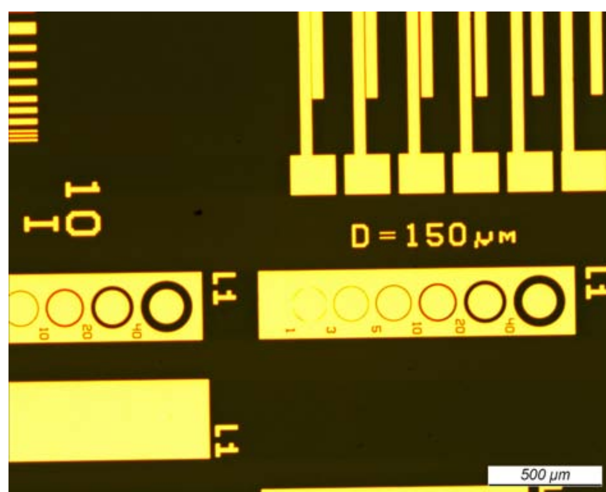

Figure 5.2: Optical microscope image of the metal structure used for cTLM measurements.

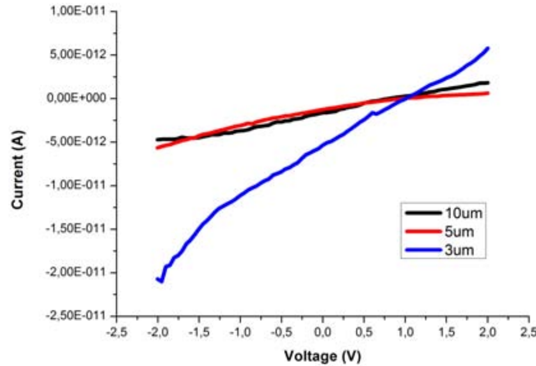

Figure 5.3: IV curve for the sample with 20% Si sputter target power at various contact spacings.

The IV curve has been collected using tungsten tips as probes and centred on the metallization using a microscope. The resulting curves can be seen in the following Fig. 5.3, 5.4, 5.5 and 5.6. The spacings are in microns.

It has to be noted that, for the sample deposited at 20% Si sputter target, the resistance is very high. This power, in fact, is just above the activation threshold for that target and hence the deposition rate is very low. This means that the film is almost stoichiometric SiO_2 with a very high resistivity. This is also the reason that prevented us to perform measurements with high spacings, limiting some of our curve to three points. From these curves, however, the resistances versus the spacings have been calculated to extract the sheet resistance. The fits can be found in Fig. 5.7, 5.8, 5.9 and 5.10.

The calculated sheet resistance versus the (relative) concentration can be found in the following Fig. 5.11:

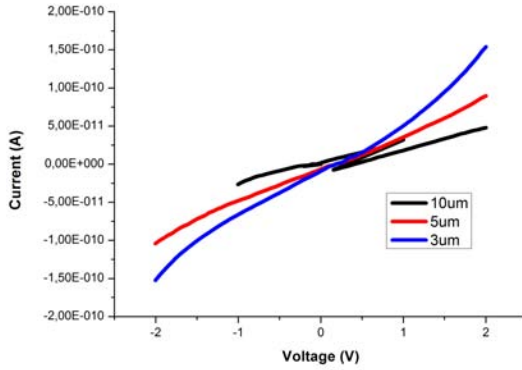

Figure 5.4: IV curve for the sample with 35% Si sputter target power at various contact spacings.

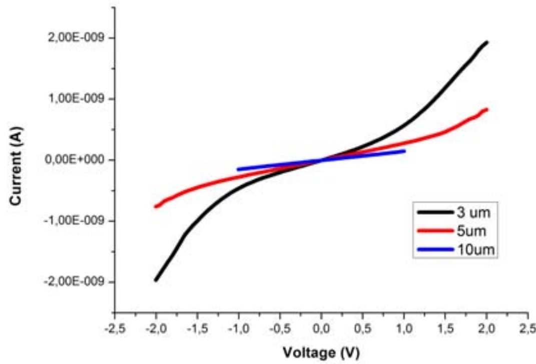

Figure 5.5: IV curve for the sample with 50% Si sputter target power at various contact spacings.

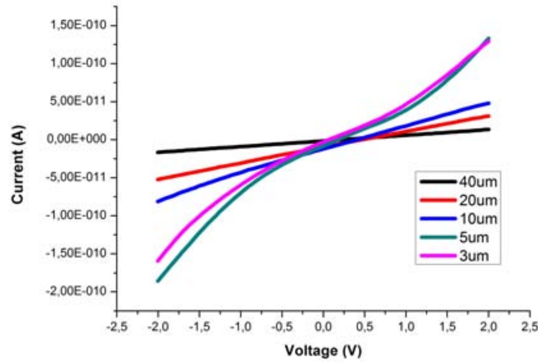

Figure 5.6: IV curve for the sample with 65% Si sputter target power at various contact spacings.

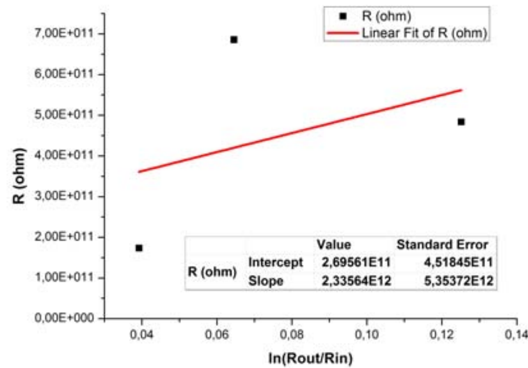

Figure 5.7: Determination of the sheet resistance for the sample with 20% Si sputter target power.

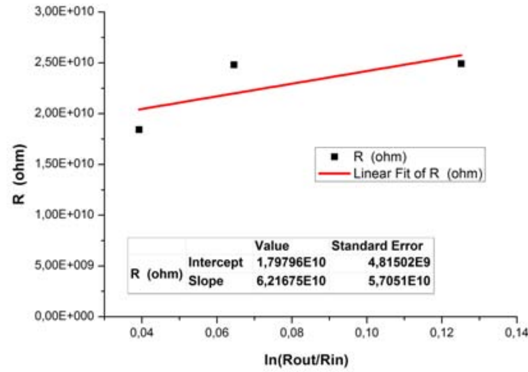

Figure 5.8: Determination of the sheet resistance for the sample with 35% Si sputter target power.

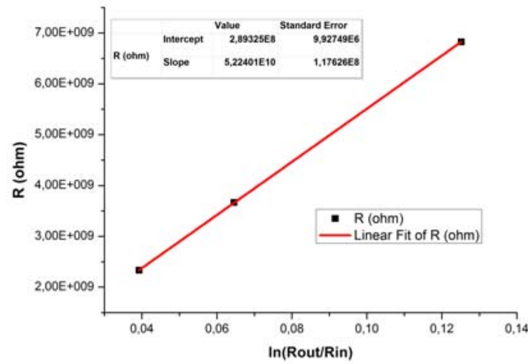

Figure 5.9: Determination of the sheet resistance for the sample with 50% Si sputter target power.

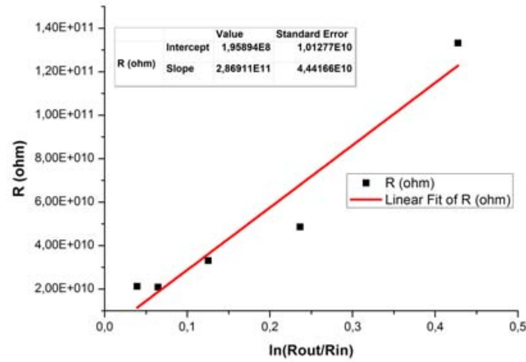

Figure 5.10: Determination of the sheet resistance for the sample with 65% Si sputter target power.

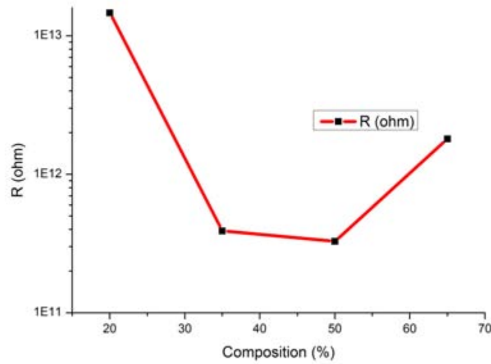

Figure 5.11: Calculated sheet resistance versus the Si sputter target power. The line is just a guide for the eyes.

Table 5.2: Description of the thick mono-layered samples.

sample	material	annealing @ 1050℃	thickness (nm)	refractive index @ 630nm
SRO1	SiO_2	no	69	1.493
SRO2	SiO_2	yes	69	1.494
SRO3	SRO Γ3	no	77	2.078
SRO4	SRO Γ3	yes	53	2.563
SRO5	SRO Γ10	no	73	1.717
SRO6	SRO Γ10	yes	62	1.882
SRO7	SRO Γ15	no	64	1.621
SRO8	SRO Γ15	yes	62	1.742

From this figure 5.11 it seems that the lowest electrical resistance can be found with a stoichiometry corresponding to a Si sputter target power of ≃40-45%. This might prove as an important indication for the deposition of films for practical purposes.

5.3 Transport in single layer thick films

The samples we used to demonstrate a change in transport mechanism with the nanostructuration are the ones summarized in tab. 5.2 We used the setup for high electric fields since the lack of ordered nanostructuration led us to consider the samples as film of dielectric material. We collected the Current-Voltage (I-V) curves in a range of ±50V with steps of 200mV with an hold time of 1s before changing the voltage. This precaution is especially important for IV curves of dielectric and in general insulating films because by varying the applied voltage to the terminals too quickly the displacement current might

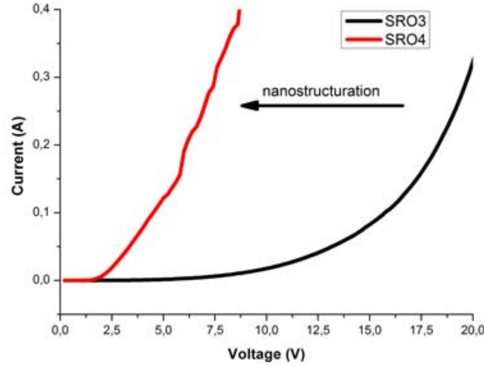

Figure 5.12: IV curves of samples SRO3 and SRO4.

be greater than the current through the film [44]. The displacement current density, in fact, is given by Eq. 5.1 :

$$J_{disp} = \epsilon \cdot \epsilon_0 \cdot \frac{dE}{dt} = \frac{\epsilon \cdot \epsilon_0}{d} \cdot \frac{dV}{dt} \tag{5.1}$$

and given the low current going through the dielectric and the usually high ϵ, this might be important and interfere with the measurements. We used a compliance current of 1A and performed only one measure for each sample because such a large current might break the dielectric film preventing further measurements. When the breakdown occurs, we disregard the remaining curve because that behaviour is no longer the one ascribed to the film.

The I-V curves of the samples are depicted in the following Fig. 5.12, 5.13 and 5.14.

We can observe some feature that emerges from the analysis of the graphs.

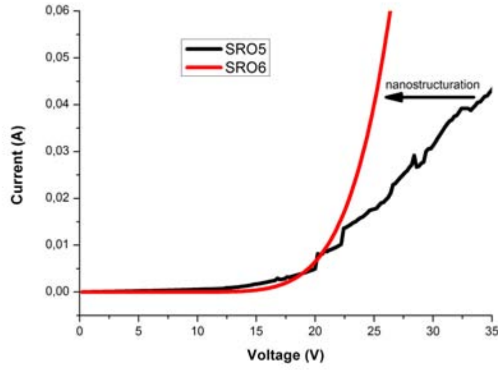

Figure 5.13: IV curves of samples SRO5 and SRO6.

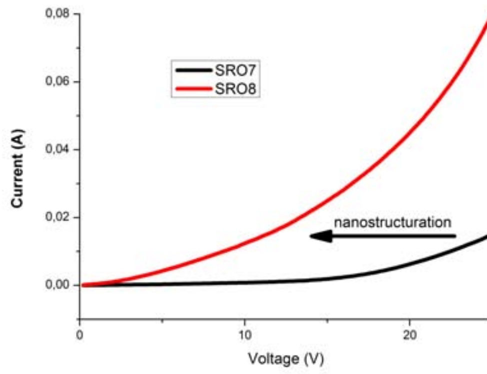

Figure 5.14: IV curves of samples SRO7 and SRO8.

The first striking features is that with nanostructuration the transport is consistently enhanced. This means that the process indeed changes going from and effective medium to a film containing what might be considered in a first approximation a defect. In the latter case current seems to be able to percolate inside the film.

The procedure to identify the transport mechanism is to fit the theoretical IV curves with the equation derived from the model and calculate one known parameter. If the value calculated in this way is completely off its theoretical value, the model can be proven false otherwise it is a candidate to describe the mechanism of that film. Of course the calculated value might not be precisely the theoretical one because in the film more than one process can happen competitively or not at the same time. Anyway if other features of the model can be observed, one can be reasonably confident of the finding.

In table 5.3 there's a (not exhaustive) list of the transport mechanism we used for the fitting of the IV curves. In this table d is the thickness of the barrier layer, Φ_B is the barrier height, m^* is the (effective) mass of the electron in the film, S is the slope of the curve from the linear fit of the expression obtained by changing the variables to the ones listed under X axis and Y axis column, T is the temperature in Kelvin, ϵ_0 is the vacuum electrical permittivity, ϵ is the relative dielectric constant of the film, $\epsilon_i = \epsilon\epsilon_0$, h is the Plank constant, q is the charge of the electron, k_B is the Boltzmann constant, $E = \frac{V}{d}$ is the electric field generated across the film from the voltage V (this assumes that the field is homogeneous inside the dielectric) and A^* is the Richardson constant.

By carefully fitting the curves with the models we discarded all the transport mechanisms except for the Poole-Frenkel emission (Fig. 5.15). With this model we can calculate a dielectric constant (for example, for SRO4) of 2 while the one measured by ellipsometry is 6. The discrepancy can be ascribed to the fact that the two values are not immediately comparable since one is the electrical dielectric

Table 5.3: Transport mechanisms.

Process	Expression	Figure		Fitting parameter
		X axis	Y axis	
Poole-Frenkel	$J \propto E \exp\left(-\frac{q\left(\Phi_B - \sqrt{\frac{qE}{\pi\epsilon_i}}\right)}{k_B T}\right)$	$\sqrt{V}$	$\ln J/V$	$\epsilon = \frac{q^3}{\pi d k_B^2 T^2 S^2 \epsilon_0}$
Fowler-Nordheim	$J = \frac{q^2 m_0}{8\pi h m^* \Phi_b} \frac{V^2}{d} \exp\left(-\frac{8\pi\sqrt{2qm^*} d \Phi_B^{3/2}}{3hV}\right)$	$\frac{1}{V}$	$\ln \frac{J}{V^2}$	$\Phi_B = \frac{3Sh}{8\pi d\sqrt{2qm^*}}$
Trap-assisted tunnelling	$I \propto \exp\left(-\frac{\pi d\sqrt{2qm^*}}{3hV} \Phi_B^{3/2}\right)$	$\frac{1}{V}$	$\ln I$	$\Phi_B = \frac{3Sh}{8\pi d\sqrt{2qm^*}}$
Schottky Emission	$J = A^* T^2 \exp\left(-\frac{q\left(\Phi_B - \sqrt{\frac{qE}{4\pi\epsilon_i}}\right)}{k_B T}\right)$	$\sqrt{V}$	$\ln J$	$\epsilon = \frac{qd}{4\pi (S k_B T)^2}$

constant, while the other is the optical dielectric constant measured in different conditions, and, as said before, more than one process can happen at the same time. Anyway the order of magnitude is the same as expected, unlike the case of the other fits that are off of several order of magnitude. Another reason that can explain the discrepancy is the freedom of choice of a parameter ξ which is reported in [45]. This parameter is found in a more general equation for Poole-Frenkel emission 5.2:

$$J \propto E \exp \frac{-q\left(\Phi_B - \sqrt{qE/\pi\epsilon_i}\right)}{\xi k_B T} \tag{5.2}$$

This parameter represents the amount of compensation present in the film, or the amount of negative traps that compensates the positive traps in the film. The case with no compensation is the usual Poole-Frenkel mechanism and is derived setting $\xi = 1$. The case of full compensation is $\xi = 2$. With this parameter, the slope is changed by a factor of $\frac{1}{\xi}$ and hence with an appropriate choice of this parameter the slope can be adjusted to give the correct dielectric constant. We did not, however, take advantage of this degree of freedom because any choice of the parameter other than the one used usually in literature ($\xi = 1$) would have been somewhat arbitrary without further evidence that could back the choice up. We just note that a value of $\xi = 1/3$ would provide a match for the dielectric constant.

Another feature that the Poole-Frenkel mechanism shows, as pointed out in [45], is that measuring the same film at different temperatures and plotting their IV curves in a Poole-Frenkel plot (i.e a plot where the logarithm of J/V is plotted against $\sqrt{V}$), one should observe a peculiar trend. The curves should, in fact, converge to a point whose voltage is related to the barrier height by Eq. 5.3:

$$\Phi_B = V\sqrt{\frac{q}{\pi\epsilon_0\epsilon_i d^2}} \tag{5.3}$$

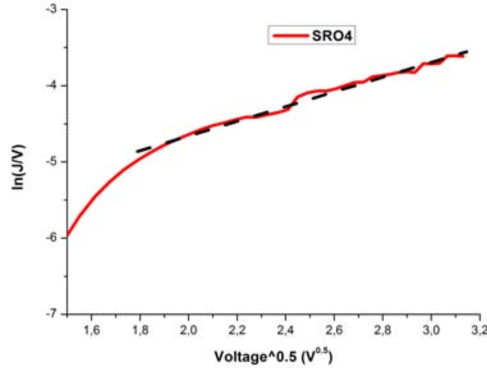

Figure 5.15: Poole-Frenkel plot for SRO4. The line is the region of the fitting.

By looking at Fig. 5.16 this behaviour can be clearly seen. Also, it is possible to see that after a certain temperature, no obvious changes in the current are detectable. This is to be expected for a thermoionic emission, where all the traps are ionized past a certain temperature. The value for this barrier height we can find is $\Phi_B \simeq 0.2$eV, which is close, but not equal, to the one reported in literature of $\simeq$1eV.

In summary, from this set of samples, we could demonstrate a change in the conduction between nanostructured and 'bulk ' SRO films, and in the case of nanostructuration, we gathered strong evidences that the Poole-Frenkel mechanism correctly describes the process happening in the samples.

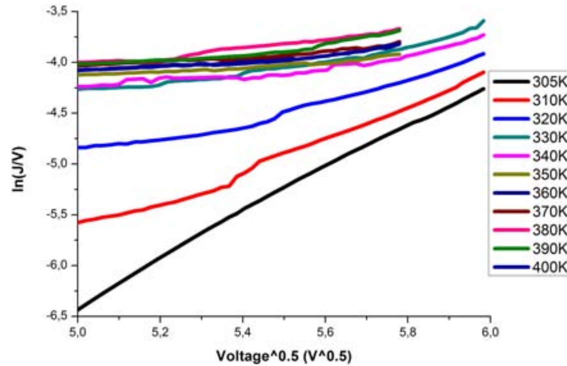

Figure 5.16: Poole-Frenkel plot for SRO4 at increasing temperature.

5.4 Transport in B-doped multi-layered films

The B-doped samples used for the identification of boron levels have been also employed for electrical measurements. The list of the samples is in Tab. 5.4: The samples have been studied with the setup for low current and at high temperature, from 300K to 400K with a step of 10K. From the top of the samples, the capping layers have been removed, but it was not possible, for obvious reasons, to remove the diffusion barrier layer of 10nm made of SiO_2 interposed between the film and the substrate. The ability to measure a current even through this layer means most likely that this layer is not as compact as a good thermal oxide, but it has some defects in it that allows the penetration of the current.

The first finding is as expected: in sample JM17 and JM18 no current can pass with a voltage up to 2V, unlike in the case of the other

Table 5.4: description of the multi-layered samples. Their substrate (obtained by etching of JM18) has also been measured.

sample	bi-layer n°	SRO thickness (nm)	SiO_2 thickness (nm)	B target power(W)
JM14	25	4	2.5	0
JM15	25	4	2.5	20
JM16	25	5	2.5	20
JM17	25	0	5+2.5	20
JM18	1	0	100	0

samples. The two samples, in fact, does not contain excess silicon and hence no nanocrystals can form in them. Hence they behave as thick insulators and no measurable current can flow through them.

From the curves of the remaining samples (JM14, JM15 and JM16) another striking feature emerges: they all strongly depend on the temperature. This behaviour led us to discard Fowler-Nordheim tunnelling and Trap Assisted Tunnelling as possible candidates, as they all are not thermally activated.

The most promising transport mechanisms that can describe the transport are Schottky emission and Poole-Frenkel emission. Since, as explained before, the Poole-Frenkel emission is enhanced by the presence of a high electric fields which does not seem to be our case as the dielectric thickness is rather high, The first one seems to be the most likely. The analogy should not be carried over too much since the films are not stoichiometric and, most importantly, are nanostructurated, making them very different from films of perfect insulators.

Having observed the temperature dependence of the IV curves of the samples, it appears to be reasonable to draw the Arrhenius plots

of the samples, to infer a first approximation of the activation energy of the process involved. From the data we selected only the points between ±0.1V, where the curves can be described in terms of straight lines. The slopes of these curves are the conductances that, suitably re-scaled to give the conducibilities ($\sigma = \frac{GL}{A}$, where G is the conductance, A is the area of the contact and L is the thickness of the film, assuming columnar conduction) can be plotted versus the (inverse of the) temperature to give the activation energy, as the following equation 5.4 states:

$$\sigma = \sigma_0 \exp^{\left(-\frac{E_a}{k_B T}\right)} \tag{5.4}$$

For each sample we have 11 points since the temperature was varied from 300K to 400K in steps of 10K. It has to be noted that the values of the conductances we can infer from the graphs are not compatible with the one predicted by a Poole-Frenkel mechanism as can be seen, i.e. in [44]. For this reason we only focused on the Schottky type mechanism [46]. We also performed measurements on a piece of substrate as control. In the following Fig. 5.17 are the Arrehnius plot of the obtained conducibilities From this plot it is apparent that the samples of SRO show two different behaviour, at low and at high temperature. It seems that the transport mechanism involved has, in fact, two different activation energies that will be derived only for JM14 because this is the only one whose experimental points allow the fitting procedure on more than two points at low temperatures. The substrate has only one slope and the so derived activation energy will be compared to the ones inferred from the samples. In Tab. 5.5 is the summary of the measurements.

In figures Fig. 5.18, 5.19, 5.20, 5.21 the IV scans for the various samples at different temperatures between 300K and 400K are reported.

To summarize all the measurements, a common way to show all the curves together is plotting the natural logarithm of the current

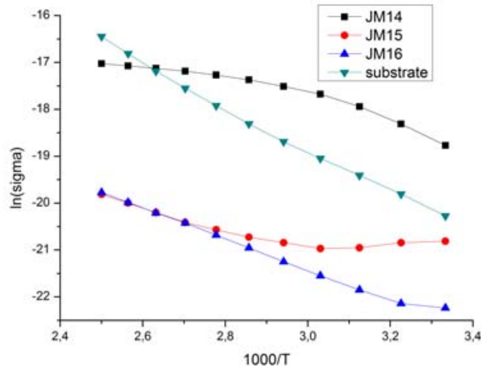

Figure 5.17: Arrehnius plot of the sample JM14, JM15, JM16 and substrate.

Table 5.5: Activation energies calculated for the multi-layered samples.

sample	E_{act}^{highT}(meV)	E_{act}^{lowT}(meV)
substrate	357	-
JM14	312	65
JM15	255	-
JM16	288	-

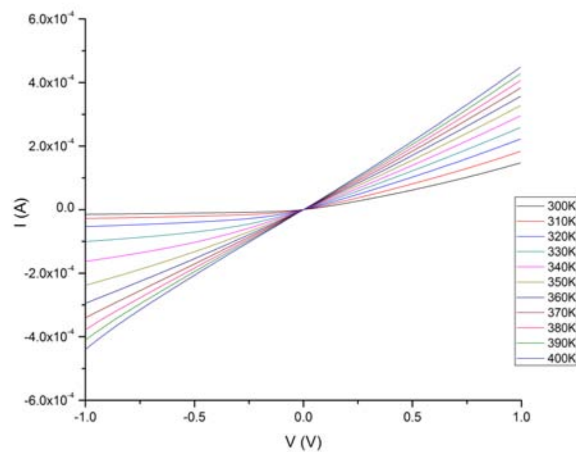

Figure 5.18: IV curve of the sample JM14.

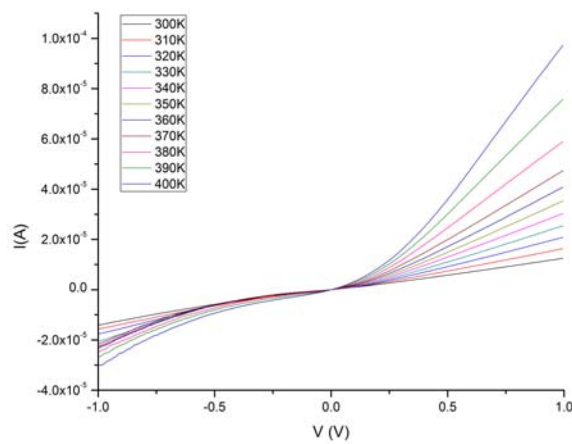

Figure 5.19: IV curve of the sample JM15.

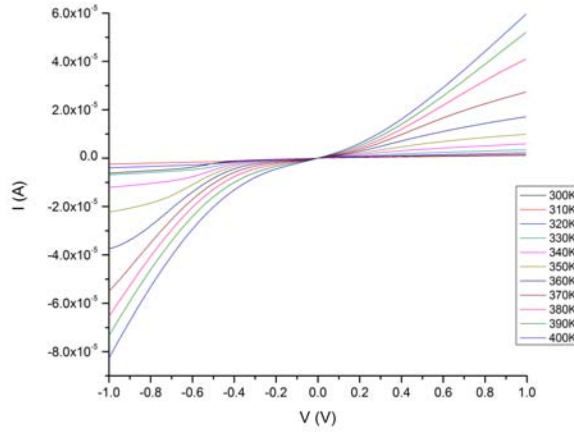

Figure 5.20: IV curve of the sample JM16.

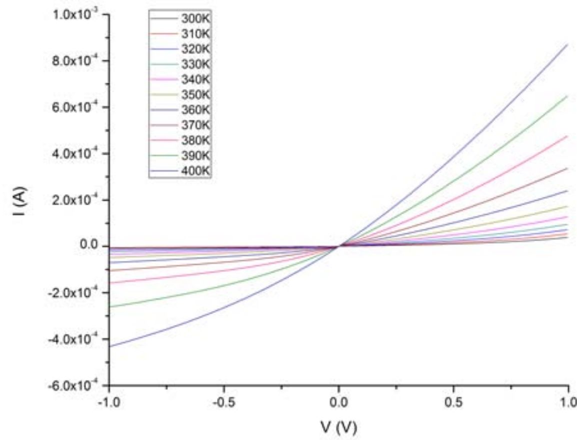

Figure 5.21: IV curve of the substrate.

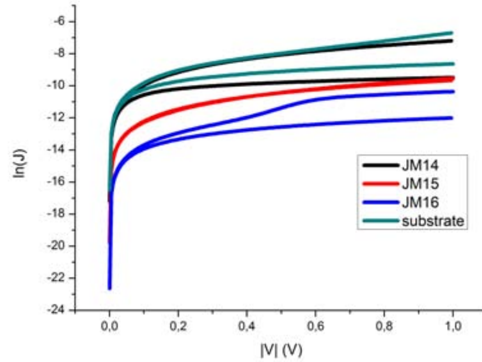

Figure 5.22: Summary of the IV curves of the samples.

density versus the absolute value of the voltage. Of course to obtain the current density it is necessary to assume a columnar transport and divide the current for the area of the contact (Fig.5.22).

The two branches of the plot for JM15 are almost indistinguishable, since (as can be seen also from Fig. 5.19) the direct and inverse characteristic for this sample are almost the same. This means that this sample is not a good rectificator unlike a diode.

Sample JM16 shows a change in slope of the upper branch, probably due to a parasitic series resistance since the behaviour is linear.

The comparison between the substrate behaviour and the samples shows that the nanostructured films behave partly as a MIS diode and partly as a metal-semiconductor junction. This is better seen comparing the activation energies in Tab. 5.5 and noticing that their order of magnitudes are comparable.

It is noteworthy that sample JM14 is the one showing a higher conductibility by three orders of magnitude compared to JM15 and

JM16. This is unexpected since the latter are doped unlike the former one which is 'intrinsic '. From Fig. 5.22 it is also apparent a worsening of the J-V characteristic with respect to JM14, This evidences, joined to the impossibility to detect boron levels as discussed previously, lead us to think that some problems with the doping occurred.

A striking feature of the curves is that JM14 conductibility is higher then the substrate by one order of magnitude at room temperature, and the current density is comparable with the one present in the substrate. This is also unexpected given the high thickness of dielectric material interposed between the contacts. This results shows that the nanostructured film does not affect the conduction by much, improving, in fact, the direct current. This is a good step in the direction of producing a solar cell with this material since the vertical conduction in such a structure plays a crucial role in the determination of the extraction efficiency of the carriers.

5.5 Transport in multi-layered films

In order to understand the transport mechanism in the configuration of QDs-based solar cell (i.e. from top to bottom), two samples specifically designed was grown from FBK. The contact mask is the same as the one depicted in fig 3.1. Only one stoichiometry, the $\Gamma = 3$ has been analysed. The difference of the two samples lies in the thickness of the SRO layer (and hence of the QDs: as the name suggests, one sample feature a SRO thickness of 15Å, the other of 30Å), as reported in Tab. 5.6. The first comparison is between the two samples.

From Fig. 5.23 it is possible to see that the sample with thinner layer is a better conductor than the other one. The possible explanation is that the silicon excess is enough for the first sample to allow a good hopping probability despite of the smaller dots, while the bigger matrix layers between adjacent dots in the second sample somehow

Table 5.6: Description of the multi-layered samples for electrical measurements.

sample	bi-layer n°	SRO thickness (nm)	SiO_2 thickness (nm)	Γ
MIL15	10	1.5	1.5	3
MIL30	10	3	1.5	3

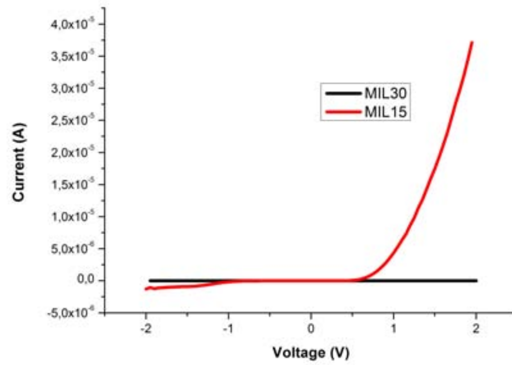

Figure 5.23: IV curves of samples MIL15 and MIL30.

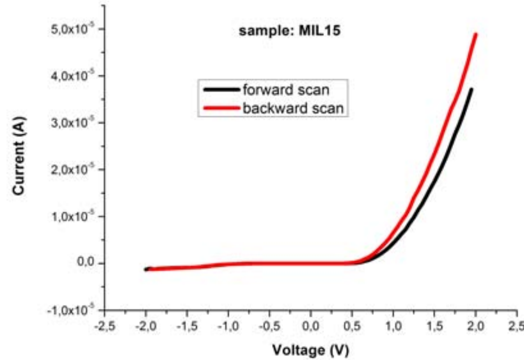

Figure 5.24: IV curve of sample MIL15 for the two scan directions.

hinder the conduction.

We performed room temperature IV scans to understand a possible effect of the direction of the scan on the characteristic. Such a feature would mean that the hysteresis could possibly be ascribed to trapped charges in the dielectric layer. For this purpose we performed very slow ramps of scanning (0.025V/s) and immediately switched the ramp from ascending to descending. The results of these measurements are depicted in Fig. 5.24

From this figure no obvious differences can be found between forward scan and backward scan. For this reason we can avoid to take into account possible wearing of the samples due to previous measurements or to age effect. Hence, from this point of view, the material is reliable for applications.

To identify the transport mechanism found in this set of samples, we performed again IV scans at different temperatures. By fitting with a straight line the region around the origin (±0.5V) we can ob-

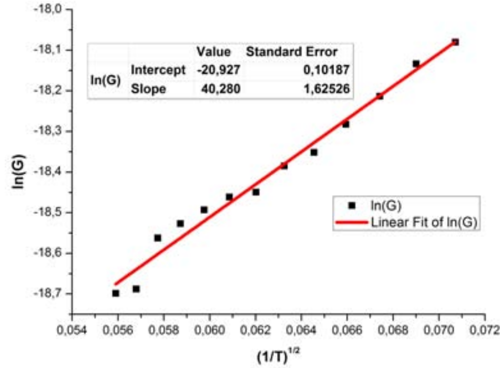

Figure 5.25: Temperature dependence of the conductance vs. the temperature.

tain the temperature dependence of the conductance (G) versus the temperature. As can be seen in the following Fig. 5.25, the values shows a pretty good agreement with a linear relationship between the logarithm of the conductance versus the inverse square root of the temperature, compatible with a hopping-percolation model as in [24].

Lastly, to further push the analogy with a solar cell, we tested the response of the samples with to the light. This is reported in Fig. 5.26 5.27

It is possible to make some considerations about the IV curve showing the differences when light is shone on the samples. First of all, we do not measure any V_{OC}, which is to be expected since no junction is present on the sample (the QDs are undoped). From Fig. 5.26 we can see that the conduction is diode-like in the dark but symmetric under illumination. This behaviour can be tentatively explained by

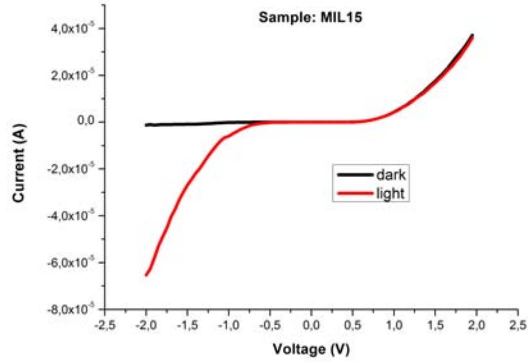

Figure 5.26: IV curve of sample MIL15, dark and under illumination.

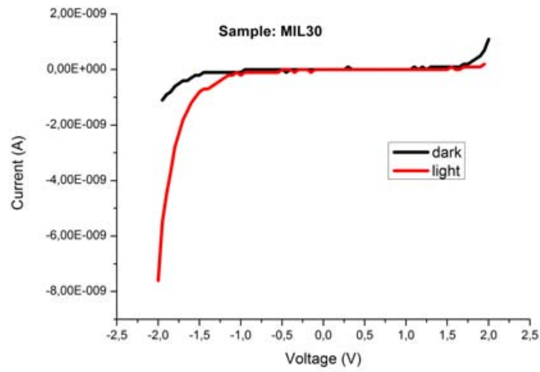

Figure 5.27: IV curve of sample MIL30, dark and under illumination.

the generation of electron-hole pairs promoted by the photons. When there is no light, the sample act as a MIS diode with an insulator layer made by the SRO. This layer does not act as a full 200 nm thick layer of oxide, rather, its composition and morphology play a crucial role in reducing the effective thickness of this layer, since a full stoichiometric layer of SiO_2 would prevent the conduction at this voltage. In this condition the nanodots probably act as filled traps and they do not participate at the conduction. When light is on, the dots might act as electron-hole couples generator (as they are intrinsic) and the conduction can be symmetric in the two verses.

We devised a model to explain this behaviour. This model can be seen in Fig. 5.28 and relies on the presence of two diodes facing the opposite direction in parallel to a single diode. The pair of diodes has a current generator and a tension generator in the middle. The first generator (I1 in the figure) represents the effect of the electrons-holes generation when light is off, the voltage generator (V1) has been added to account for the tension generated by the charging of the traps that are present in the film. This is confirmed from the measurements as a function of the temperature, that we interpreted with an Hopping-Percolation model which is, of course, promoted by traps. The single diode (D1) models the effect of the MIS structure of the sample with no light. The two diodes (D2 and D3) mimic the effect of the conduction between QDs in the two directions, depending on the polarization: since we assume a pair is generated, there is no preferential polarization that allows the current to pass. This just models the film as an 'effective ' pair of diodes instead of describing each possible route of a carrier between QDs of varying distance. All the parallel resistances have been included to simulate the parasitic paths of conduction that might be present in the film.

This model explains the symmetric IV curve and the difference with light on (see Fig. 5.30). This also allows us to model the voltage threshold shift of the characteristic in inverse polarization of the IV

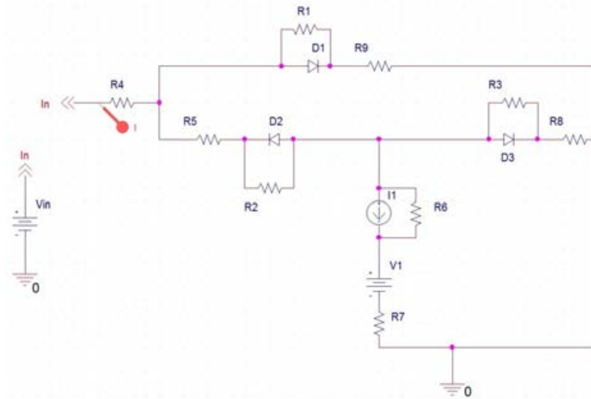

Figure 5.28: Equivalent circuit that models the conduction in the multi-layered samples.

curve as visible from the position of the arrows in Fig. 5.29 and Fig. 5.30 as compared to the close-up IV curve from sample MIL15 visible in Fig. 5.31. It has to be remarked that the numbers visible in the figures are not the results from a fitting of a simulated IV curve with the value of the resistances as parameters. These figures just show the qualitative behaviour of the IV curve of such a simplified model. Real values can be obtained from multi-parametric fits, but this analysis has not be performed here.

A possible improvement of this model is the addition of several others parallel diodes pairs with increasing series resistance to simulate the hopping between QDs further away than the closest ones. Also the addition of a proper capacitance instead of the voltage generator might be considered if the charging, the transient and the Capacitance-Voltage (CV) characteristics are to be modeled as well.

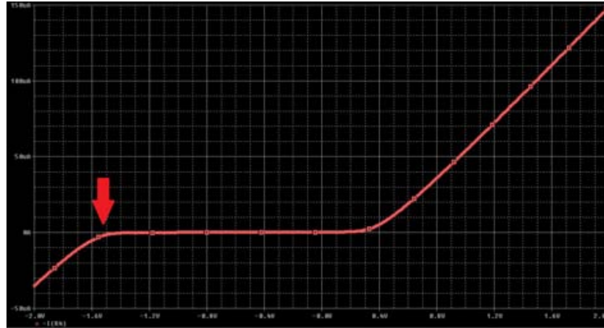

Figure 5.29: Simulated IV curve from the model reported in Fig. 5.28 with I1 off (dark).

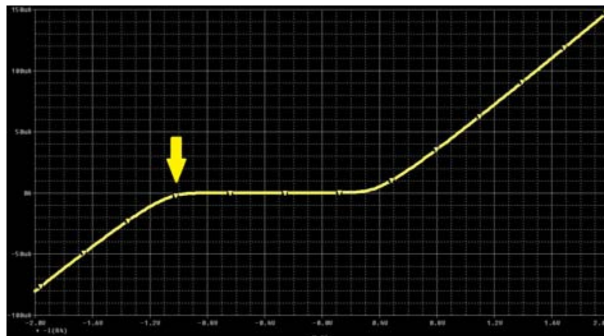

Figure 5.30: Simulated IV curve from the model reported in Fig. 5.28 with I1 generating current (illuminated).

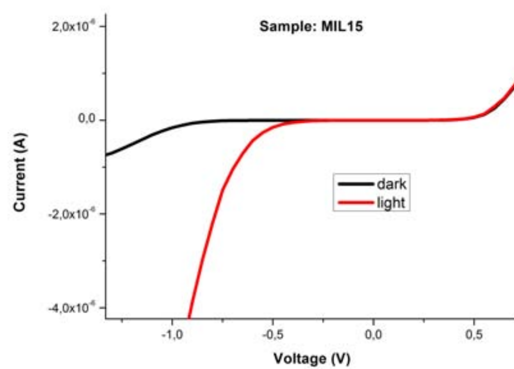

Figure 5.31: Close-up of the IV curve of sample MIL15.

Chapter 6

All-silicon Quantum Dot-based Photovoltaic Device

The apex of the work on all-silicon quantum dot-based photovoltaics is the realization of a full working device that exhibits the gap opening and a good current extraction. In this chapter, one of the latest work on this aspect will be presented. In the first section, the state of the art of this technology will be presented, reviewing the work done in [47]. The last part about External Quantum Efficiency (EQE) and IV measurements under solar simulator is the description of the work we performed on a sample grown by the same laboratory in [47] with the same structure of the device presented in their work.

6.1 Previous work

6.1.1 Deposition

In [47] one of the first fully functional PV device made of nanostructured SRO layers is described. A p-i-n structure were fabricated by sputtering, on a quartz substrate, alternate layers of SiO_2 and SRO and cosputtering, where appropriate, either B or P to create the junction. A 1100℃ anneal for 1h was used to nucleate QDs, followed by an hydrogen plasma anneal at 625℃. A Reactive Ion Etching (RIE) in CF_4:O_2 was used to isolate B-doped mesas and expose the underlying P-doped part. To do so, a patterned metal mask has been deposited that served also as ohmic contact for the electrical measurements. To cover as much as possible of the P-doped part with metal for the other contact, aluminium was evaporated just after the RIE steps. Due to the poor step coverage of the evaporation process, the top contact on the B-doped part served also as a shadow mask for the evaporated aluminium. To prevent shot-circuits, this second metal deposition was kept very thin, nevertheless, most of the device resulted shorted and only small area of it was useful for the measurements. In Fig. 6.1 is a scheme of the section of the sample.

6.1.2 Current-Voltage measurements

The IV characteristic of this device has been measured. As visible in Fig. 6.2 the self alignment, while helpful to reduce the series resistance, was not enough for the illuminated curve not to be limited by a resistance of 28 kΩcm^2. Nevertheless, the 492mV V_{OC} measured is the highest for Si-nc based solar cells on insulating substrate. The dark IV curve of the device shows, instead, a series resistance of 4.1kΩcm^2, obtained considering the different geometry of this sample with a regular p-n diode.

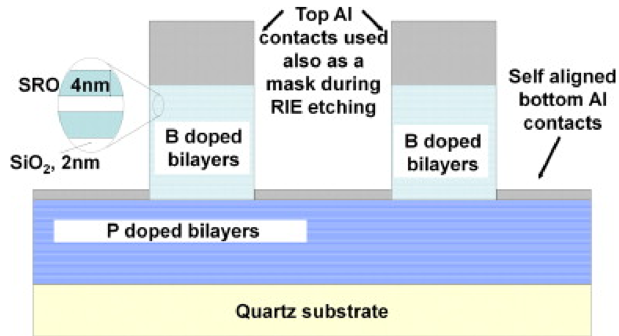

Figure 6.1: scheme of the section of the device. Image taken from [47].

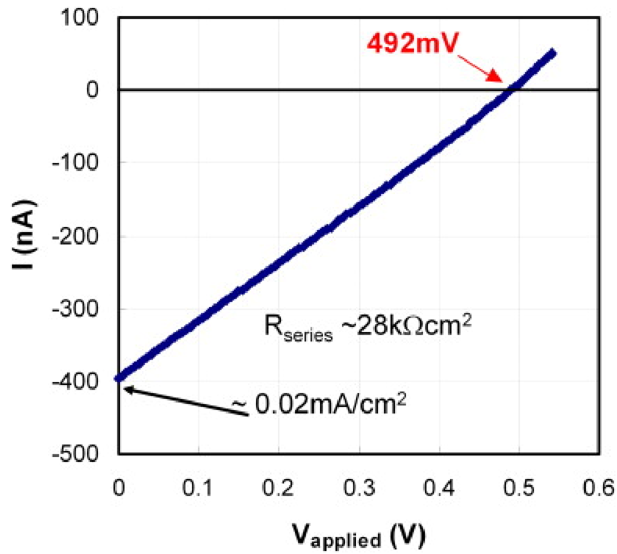

Figure 6.2: Illuminated IV curve of a 2.2mm^2 device. Image taken from [47].

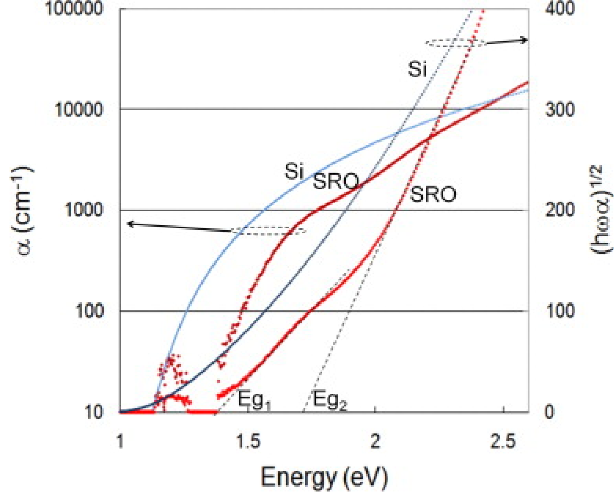

Figure 6.3: Tauc-plot of the film composing the device. Image taken from [47].

6.1.3 Optical characterization

The absorption coefficient of this structure was measured with an Universal Reflectance Accessory (URA) and a spectrophotometer. By employing particular care in the measurements of the reflectance (R) and transmittance (T), it was possible to extract a very precise Tauc plot of the film.

The analysis of the plot in Fig. 6.3 allows to identify two different behaviours and hence two different band gaps of E_{g1}=1.4 eV and E_{g2}=1.7 eV. This observation justify the tentative model of the device that will be described in the following section.

6.1.4 Model describing the device

The presence of two distinct behaviour in the optical absorption coefficient and the striking difference in the series resistance between illuminated and dark IV curve suggest the use of a two-diodes model to qualitatively explain the device characteristic. The authors propose the presence of a diode with no PV response (a 'dark' diode) and one, smaller, with it (the 'light' diode) and featuring the observed 492mV V_{OC}. The two diodes are in parallel and, in series with each one, there is a series resistance equal to the one measured in each case The presence of this two diodes is explained by the presence of a region where mobility and life-time are very low (the dark diodes) and a region (a smaller part of the device) with a PV response.

This model fits the experimental data well, but the real use of it will be the determination of the two bandgaps by measuring the IV curves (both dark and light) as a function of the temperature. This measure will tell if the gap opening really takes place in such a material or not. This analysis has not been performed yet since the presence of quartz prevents the thermalization of the film. For this purpose, another stage with electrical contact on the temperature-controlled plate will be needed.

6.2 Experimental results

Another sample grown in the same conditions as the one described in Fig. 6.1 has been prepared by UNSW and sent to us to perform External Quantum Efficiency (EQE) and IV measurements. The chip features several devices of different areas. We measured two devices, each one having an area of 4.4mm^2 with fingers spaced 50μm apart (Fig. 6.4). . A commercial spectral response system (Fig 6.5) from ReRa Solutions has been used to measure the EQE.

Figure 6.4: Microscope image of the device measured.

Figure 6.5: The spectral response system used in this work.

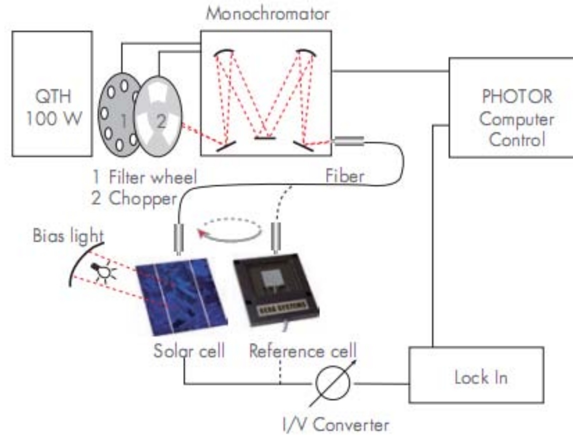

Figure 6.6: Schematics of the spectral response system used in this work.

The system features a 100W halogen lamp, a Lot-Oriel single monochromator with three grids to cover a range from 250 nm to 1800 nm, a Melles-Griot 10^9 gain 1pA minimum detectable current pre-amp, and a Stanford Research SR830 digital lock-in amplifier coupled with a chopper with interchangeable heads to cover the frequency range from 1Hz to 1kHz. The sample chamber is equipped with 3 different lights of tunable intensities to be used as bias: a white halogen lamp, a 3 W blue (470 nm) led and a 3 W IR (810 nm) led (see schematics in fig. 6.6). To contact the electrodes deposited on the film, tungsten tips attached to micro-manipulators have been employed.

To the best of our knowledge, no measurements of this kind have been performed before on multi-layered, doped samples on quartz, possibly because of the inherently low currents. With our system we were able to measure the EQE of such a film in various conditions such as varying the frequency of the chopper or by applying different

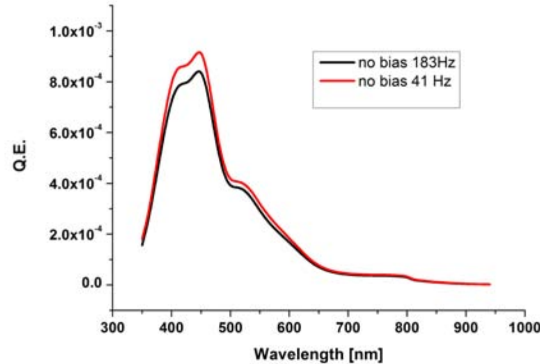

Figure 6.7: EQE of the sample at different chopping frequencies.

light bias. In Fig. 6.7 it is possible to see the effect of the frequency of the chopped light on the EQE. Comparing the two curves, we can see that there is some capacitive effect since the curve corresponding to the lower frequency (41Hz) is higher than the one measured at higher frequency (183Hz). Anyway, since the shapes of the curves are the same, as can be demonstrated by performing the ratio of the two curves, we performed further measurements at low frequency given the higher signal obtained in this condition. The curve labelled 'Device 2' in Fig. 6.8 is from another device on the same chip and it demonstrates a good uniformity of the deposition since, again, the two curves show the same shape.

A noteworthy feature that emerges from the figure is that the EQE is a function of the illumination used as bias while scanning with the monochromatic light as can be seen in Fig. 6.9. In particular, the measured EQE decreases when light is shone on the sample.

By performing IV scans with different illumination, we can derive

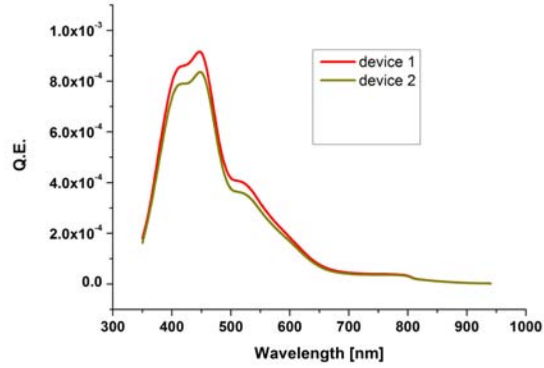

Figure 6.8: EQE of two devices on the same chip.

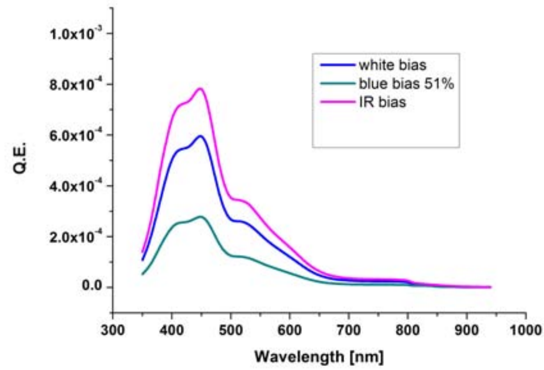

Figure 6.9: EQE of the device with different illumination intensities.

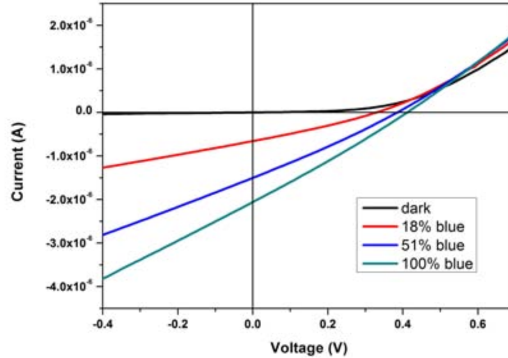

Figure 6.10: IV scans at different illumination intensities.

further insight about this aspect. The measurements reported in fig. 6.10 are made using the blue led bias at different intensities. This figure shows that it is the shapes of the IV curves themselves that changes, not only the I_{SC}s (which, of course are increasing with the intensity). The fill factors of these curves are clearly dropping with the illumination.

The reason behind this behaviour is that, given the very high series resistance of the device (which, measured fitting the linear part of the IV curves at high voltage, results 168 $k\Omega$ and 148 $k\Omega$ in the dark and under illumination respectively) shifts the operating point of the device far from the short circuit conditions. Under no light bias, the current measured are of the order of the nA that, multiplied with the series resistance we measure, gives a voltage drop of the order of 10 mV. This does shift the operating point of the device from the short circuit conditions, but not by much. When a bias is applied the current is higher and, at that point, the voltage drop makes the device work

far away from short circuit, in fact close to open circuit.

Looking at the equivalent circuit proposed in [47] and in [48], there is no electrical bias that could be applied to the device that would shift the operating point of the device in short circuit conditions. There have been some debate if this EQE can be called 'the EQE of the diode', but , since shining light on the device let us collect a photocurrent it is probably safe to call this 'the EQE of the device' since the series resistance is unavoidable in this configuration. Furthermore, since under 1-sun illumination the voltage drop across the diode will always be the same and since the circuit is externally in short circuit, we can refer to what we measure under 1-sun illumination bias as the 'EQE'.

For this reason we performed an IV scan under simulated 1 sun illumination to assess the performance of the solar cell. For this purpose, a solar simulator from Oriel with a 450W Xe lamp and filters suitable to simulate AM1.5G spectrum has been used. The results (visible in Fig. 6.11) are encouraging, even though the figures of the efficiency are far from impressive (0.003%). It has to be noted that the V_{OC} of his device is lower than the one reported in [47] even though the preparation is the same. This is expected because the two samples come from different batches and the reproducibility of the deposition has yet to be confirmed. To check the correctness of our analysis we performed the calculation of the J_{SC} that the cell should produce using the tabulated 1 sun AM1.5G solar spectrum. The calculation has been performed using the EQE resulting from the application of the blue bias at 50% of the power. This choice is justified by the fact the the I_{SC} measured in this case is almost equal to the one measured under the solar simulator, possibly indicating that the injection level in the spectral range of the sensitivity of the cell is approximately equal in the two scenarios.

Using as the area of the active surface the full 4.4mm^2 of the device, the calculated current is off by a factor of ten with respect of the

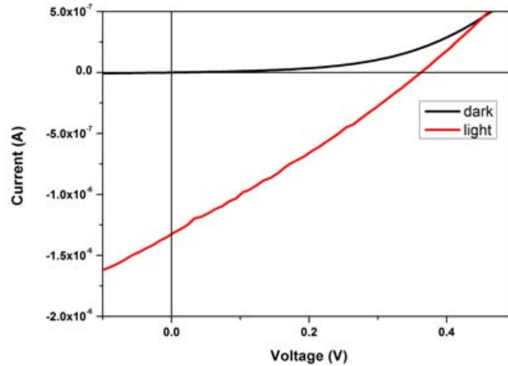

Figure 6.11: IV scan under simulated 1 sun illumination

measured one. Assuming the model in [47] is correct, we assumed the area of the dark diode to be the whole area of the device and the area of the light diode to be equal to the dark diode one times the ratio of the two series resistance (the dark and the light one). This gives the value of 3.88mm^2 for the light diode as opposed to the full 4.4mm^2 of the dark diode (i.e. a variation of $\simeq$15%). The measured value (34μA/cm^2) are just a factor 4 away from the calculated one (144μA/cm^2), but this analysis assumes no variation of the resistivity. By using the area covered with QDs (approximately half of the whole surface) the two current differ by just a factor of 2.

It is clear that no precise calculation can be performed at this stage as they all are very sensitive to the choice of the area and of the resistivity, but, given the uncertainties inherent to this analysis, these results are remarkable.

Lastly, we measured the reflectance of the sample using the accessory which is included in the spectral response system and an in-

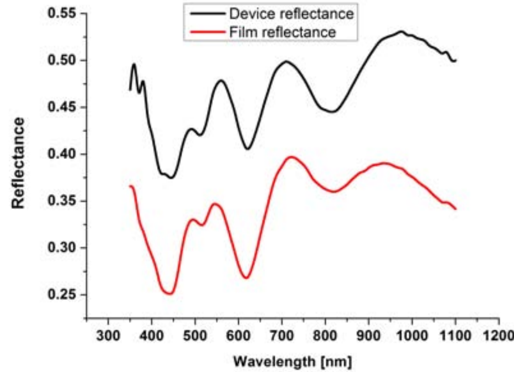

Figure 6.12: Reflectance of the sample.

tegrating sphere and the transmittance with an UV-VIS-NIR spectrophotometer. We performed two measurements, one directly on top of the device we use for the EQE and the IV scans, another one onto a region of the sample with less metal, to discriminate the two contributions. The reflectance measurements are reported in Fig. 6.12. Using these spectra, we could derive a very first approximation of the Internal Quantum Efficiency (IQE) of the film, which is reported in Fig. 6.13, by using the equation $A = 1 - R - T$, where A is the absorption coefficient.

These results are encouraging and it is safe to say that the first step leading to the realization of a all-Si QDs-based solar cell has been made.

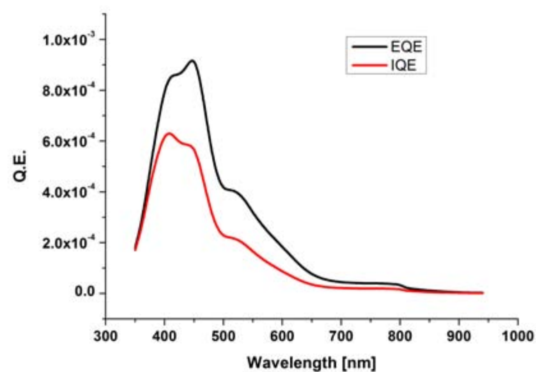

Figure 6.13: EQE and IQE of the device.

Chapter 7

Conclusions

In my thesis I studied nanostructured silicon rich oxide for photovoltaic applications. This material aims to be part of the solution of the energy shortage problem that the world is facing thanks to a possible reaching of efficiencies greater than 40% using inexpensive material. To achieve this goal a long work is needed and the comprehension of the complicated processes at work in this material is fundamental.

A tandem solar cell based on SRO requires the ability to tune the band-gap of the material at will, to be able to dope the nanocrystals thus forming a junction and to efficiently collect the photo-generated charges. In this work I focused my research over the issue of doping and of the electrical transport and of the implementation of a standard procedure to assess the stoichiometry of silicon-rich oxide films.

From my work, it appears that the ability to dope the dots is a big issue, since no clear evidences of the doping and of the enhancements of the conductivity was found. Nevertheless the measurements performed on a prototype device made with this material, showed a diode like behaviour, indicating that a doping-like effect is taking place.

The nanostructuration, on the other hand, does have a big impact on the conduction, making the transport in such a film possible. In

particular, Poole-Frenkel thermionic emission seems to be the dominant mechanism that makes this material conductive.

The multi-layered structure also plays an important role in determining the electrical properties of the samples, since the conduction in this case seems to change to percolation or hopping and the samples start to have a clear photoresponse. To get further insight of the samples, an equivalent circuit have been proposed and it seems to be appropriate in explaining the features showed by the characteristic IV curve of the device.

Finally, a working solar cell made only of SRO has been analysed. This device is remarkable in that it shows a photovoltaic effect and an EQE can be measured. This is completely different than the one of regular c-Si solar cell and, given the lack of a semiconductor substrate, it can only be ascribed to the junction formed by the doped quantum dots. Several EQE and IV measurements have been performed on this device and some very interesting features (such as the dependency of the EQE from the illumination intensity) have been studied.

In the near future it will be needed to study the reliability and reproducibility of this kind of system, possibly solving the problem of the very high series resistance of the film and it will be needed to deposit other SRO layers embedding QDs of different dimensions to demonstrate whether it is possible to design at will the EQE and exploiting the solar spectrum at its maximum potential.

Chapter 8

Acknowledgments

This work has been done thanks to the help of several people. Without them, my Ph.D. would have been very different and much harder.

I would like to thank all the people from ARC Photovoltaic Centre of Excellence where I spent 3 months of work and fun. Of all of them, Dr. Ivan Perez-Wurfl, Prof. Gavin Conibeer, Prof. Martin Green and Tian Zhang have all made my time there very productive and very pleasant and it is a pleasure for me to thank them in particular.

Dr. Georg Puker from FBK and Prof. L. Pavesi from Trento University helped me a lot and provided me with several samples, thanks for the long discussions over the data and for the commitment.

Dr. Simona Binetti and Dr. Maurizio Acciarri made this thesis and the whole doctorate possible. They guided me, helped me, taught me and pushed me to learn new things. Should I say more?

Dr. Gianfranco Cerofolini has always found time for me and helped me whenever I was in doubt (which happened frequently enough). Thanks GF.

Least but not last, my colleagues Andrea Scaccabarozzi, Alessia Le Donne, Stefano Marchionna, Elisabetta Romano, Lorenzo Caccamo, Bruno Lorenzi, Andrea Finto and Silvia Trabattoni. They was with

me all the time during these years. Also, lunch time would have been very boring without them!

Chapter 9

Publications list

Paper: M. Morgano, T. Zhang, I. Perez-Wurfl, S. Binetti, M. Acciarri, G. Conibeer, Assessment of the composition of Silicon-Rich Oxide films for photovoltaic applications by optical techniques. Energy procedia (2011), in press.

Paper: M. Acciarri, A. Le Donne, M. Morgano, L. Caccamo, L. Miglio S. Marchionna, R. Moneta, M. Meschia, S. Binetti Hybrid sputtering/evaporation deposition of Cu(In,Ga)Se2 thin film solar cells, Energy procedia (2011) , in press.

Paper: Morgano, M. Perez-Wurfl, I. Binetti, S., Nanostructured Silicon-Based Films for Photovoltaics: Recent Progresses and Perspectives, Science of Advanced Materials, Volume 3, Number 3, June 2011 , pp. 388-400(13).

Poster: M. Morgano, T. Zhang, I. Perez-Wurfl, S. Binetti, M. Acciarri, G. Conibeer, Assessment of the composition of Silicon-Rich Oxide films for photovoltaic applications by optical techniques, EMRS 2011 (Nice, France).

Poster: M. Acciarri, A. Le Donne, M. Morgano, L. Caccamo, L. Miglio S. Marchionna, R. Moneta, M. Meschia, S. Binetti Hybrid sputtering/evaporation deposition of Cu(In,Ga)Se2 thin film solar cells,

EMRS 2011 (Nice, France).

Oral Presentation (with poster): M. Morgano, A. Scaccabarozzi, S. Binetti, M. Acciarri, Z. Yuan, G. Pucker, and L. Pavesi, Electrical-transport mechanism for silicon quantum-dot-based solar cells, CIMTEC 2010 (Montecatini, Italy).

List of Figures

1.1 Shockley-Quaisser efficiency limits as a function of bandgap. 7
1.2 Schematic design of a tandem solar cell. 7
1.3 Calculated maximum theoretical efficiencies for various scenarios. 8

2.1 Proposed design for an all-Silicon tandem solar cell. . . 12
2.2 TEM images of a multi-layered nanostructured SRO structure (left) and of a single nanocrystal (right). . . . 13
2.3 Measured (dots) and calculated (lines)PL energy as a function of dot diameter. 14
2.4 XRD spectra of samples with different levels of doping showing the effects of dopants on QDs dimensions. . . . 19
2.5 Formation energy of neutral impurities at the center of a Si-QD as a function of inverse radius for B atoms (left) and P atoms (right). Inverse radius equal to zero is the bulk value. 20
2.6 Formation energy of neutral impurities as a function of impurity position in the QD. 21

3.1 Layout of the metal mask used to deposit electrical contacts. 23

3.2 TEM image of a sample analogous to the one described in this section. 23
3.3 Schematics of the sample section. 24

4.1 Thickness calibration curve. 30
4.2 Calculation of the etch rate of a solution 1% vol. 31
4.3 Calculation of the stoichiometry from FTIR measurements. 33
4.4 Calculation of the stoichiometry by UV-VIS measurements. 35
4.5 Correlation between UV-VIS and FTIR measurements. 35
4.6 Spectra of samples JM8-JM13. The peaks ascribed to boron are marked with arrows. 37
4.7 Spectra of samples JM8-JM13. In JM11 the peaks of boron are also visible. 38

5.1 Picture of the sample holder. In this figure the tungsten tip and the electrical connections are clearly visible. . . 43
5.2 Optical microscope image of the metal structure used for cTLM measurements. 45
5.3 IV curve for the sample with 20% Si sputter target power at various contact spacings. 46
5.4 IV curve for the sample with 35% Si sputter target power at various contact spacings. 46
5.5 IV curve for the sample with 50% Si sputter target power at various contact spacings. 47
5.6 IV curve for the sample with 65% Si sputter target power at various contact spacings. 47
5.7 Determination of the sheet resistance for the sample with 20% Si sputter target power. 48
5.8 Determination of the sheet resistance for the sample with 35% Si sputter target power. 48

5.9 Determination of the sheet resistance for the sample with 50% Si sputter target power. 49
5.10 Determination of the sheet resistance for the sample with 65% Si sputter target power. 49
5.11 Calculated sheet resistance versus the Si sputter target power. The line is just a guide for the eyes. 50
5.12 IV curves of samples SRO3 and SRO4. 52
5.13 IV curves of samples SRO5 and SRO6. 52
5.14 IV curves of samples SRO7 and SRO8. 54
5.15 Poole-Frenkel plot for SRO4. The line is the region of the fitting. 55
5.16 Poole-Frenkel plot for SRO4 at increasing temperature. 56
5.17 Arrehnius plot of the sample JM14, JM15, JM16 and substrate. 58
5.18 IV curve of the sample JM14. 59
5.19 IV curve of the sample JM15. 59
5.20 IV curve of the sample JM16. 60
5.21 IV curve of the substrate. 60
5.22 Summary of the IV curves of the samples. 61
5.23 IV curves of samples MIL15 and MIL30. 62
5.24 IV curve of sample MIL15 for the two scan directions. . 63
5.25 Temperature dependence of the conductance vs. the temperature. 64
5.26 IV curve of sample MIL15, dark and under illumination. 64
5.27 IV curve of sample MIL30, dark and under illumination. 65
5.28 Equivalent circuit that models the conduction in the multi-layered samples. 66
5.29 Simulated IV curve from the model reported in Fig. 5.28 with I1 off (dark). 66
5.30 Simulated IV curve from the model reported in Fig. 5.28 with I1 generating current (illuminated). 67
5.31 Close-up of the IV curve of sample MIL15. 67

6.1 scheme of the section of the device. Image taken from [47]. 70
6.2 Illuminated IV curve of a 2.2mm^2 device. Image taken from [47]. 71
6.3 Tauc-plot of the film composing the device. Image taken from [47]. 71
6.4 Microscope image of the device measured. 72
6.5 The spectral response system used in this work. 73
6.6 Schematics of the spectral response system used in this work. 74
6.7 EQE of the sample at different chopping frequencies. . 74
6.8 EQE of two devices on the same chip. 75
6.9 EQE of the device with different illumination intensities. 76
6.10 IV scans at different illumination intensities. 76
6.11 IV scan under simulated 1 sun illumination 77
6.12 Reflectance of the sample. 78
6.13 EQE and IQE of the device. 79

List of Tables

3.1 Description of the thick mono-layered samples. 24
3.2 Description of the multi-layered samples. The horizontalline divides the samples coming from the two annealing batches as explained in the text 25
3.3 Description of the multi-layered samples for electrical measurements. 26
3.4 Description of the samples for stoichiometry assessment. 27

4.1 Summary of the measurements of the samples for stoichiometry assessment. 34
4.2 Description of the multi-layered samples. 37

5.1 Description of the samples for IV measurements with different stoichiometries. 44
5.2 Description of the thick mono-layered samples. 51
5.3 Transport mechanisms. 53
5.4 description of the multi-layered samples. Their substrate (obtained by etching of JM18) has also been measured. 56
5.5 Activation energies calculated for the multi-layered samples. 58

5.6 Description of the multi-layered samples for electrical measurements. 62

Bibliography

[1] W. Shockley and H. J. Queisser, J. Appl. Phys. 32, 510 (1961).

[2] Green, M. A., Emery, K., Hishikawa, Y., Warta, W. (2010). Solar cell efficiency tables (version 35). Online, (version 35), 144-150.

[3] Antonio Marti, Gerardo L. Araujo, Limiting efficiencies for photovoltaic energy conversion in multigap systems, Solar Energy Materials and Solar Cells, Volume 43, Issue 2, 1995.

[4] Harrison, P. Quantum well, wiresand dots: theoretical and computational physics, John Wiley & Sons Ltd, Chisester (2000)

[5] Meillaud, F., Shah, A., Droz, C., Vallat-Sauvain, E., and Miazza, C. Sol. Energy Mater. Sol. Cells, 90, 29522 (2006).

[6] S. Tiwari, F. Rana, H. Hanafi, A. Hartstein, E. F. Crabbe, and K. Chan, Appl. Phys. Lett. 68, 1377, (1996).

[7] M. Porti, M. Avidano, M. Nafria, X. Aymerich, J. Carreras, O. Jambois, and B. Garrido, J. Appl. Phys. 101, 064509 (2007).

[8] T. Z. Lu, M. Alexe, R. Scholz, V. Talalaev, R. J. Zhang, and M. Zacharias, J. Appl. Phys. 100, 014310 (2006).

[9] S. Ossicini, L. Pavesi, and F. Priolo, Light Emitting Silicon for Micro- Photonics, Springer Tracts in Modern Physics Vol. 194 Springer-Verlag, Berlin, (2003).

[10] Iacona, F.; Irrera, A.; Franz, G.; Pacifici, D.; Crupi, I.; Miritello, M. P.; Presti, C. D.; Priolo, F.; IEEE Journal of Selected Topics in Quantum Electronics, vol. 12, 6, 1596 - 1606 (1996).

[11] R. J. Walters, G. I. Bourianoff, and H. A. Atwater, Nat. Mater. 4,143 (2005).

[12] D. Di, I.Perez-Wurfl,G.Conibeer,M.A.Green, Sol. En. Mat. and Sol. Cells, 94, 2238-2243, (2010)

[13] Daldosso, N., Das, G., Larcheri, S., Mariotto, G., Dalba, G., Pavesi, L. (2007). Silicon nanocrystal formation in annealed silicon-rich silicon oxide films prepared by plasma enhanced chemical vapor deposition, 1-7.

[14] Hossain, S. M., Anopchenko, A., Prezioso, S., Ferraioli, L., Pavesi, L., Pucker, G. (2008). Subband gap photoresponse of nanocrystalline silicon in a metal-oxide-, 2-5.

[15] Hao, X. J., Podhorodecki, A. P., Shen, Y. S., Zatryb, G., Misiewicz, J., Green, M. A. (2009). Effects of Si-rich oxide layer stoichiometry on the structural and optical properties of Si QD / SiO 2 multilayer films, 485703.

[16] S. K. Shrestha, P. Aliberti, G. J. Conibeer, En. Mat. and Solar Cells, Vol. 94, 9, 1546-1550, (2010)

[17] B. Puthen-Veettil, D. König, G. Conibeer, En. Procedia, 2, 1, (2010).

[18] C.R. Crowell, The Richardson constant for thermionic emission in Schottky barrier diodes, Solid-State Electronics, Volume 8, Issue 4, April 1965, Pages 395-399

[19] J. Frenkel, Tech. Phys. USSR 5, 685 (1938).

[20] J. Frenkel, Phys. Rev. Lett., 54, 647 (1938).

[21] R. H. Fowler, L. Nordheim, Proc. of the Royal Society of London, 119, 173-181 (1928).

[22] M. Lenzlinger, E. H. Show, J. Appl. Phys., 40, 278-283 (1969).

[23] M. P. Houng, Y. H. Wang, W. J. Chang, J. Appl. Phys., 86, 1448, (1999).

[24] E. Ŝimánek, The temperature dependence of the electrical resistivity of granular metals, Solid State Communications, Volume 40, Issue 11, December 1981, Pages 1021-1023, ISSN 0038-1098, 10.1016/0038-1098(81)90059-4.

[25] C.-W. Jiang, et al., Resonant tunneling through defects in an insulator: modeling and solar cell applications, J. Appl. Phys. 96 (2004) 50065012.

[26] Solid Solubility and Diffusion Coefficients of Boron in Silicon, G. L. Vick and K. M. Whittle, J. Electrochem. Soc. 116, 1142 (1969)

[27] X.J. Hao, E-C. Cho, C. Flynn, Y.S. Shen, S.C. Park, G. Conibeer, M.A. Green, Synthesis and characterization of boron-doped Si quantum dots for all-Si quantum dot tandem solar cells, Solar Energy Materials and Solar Cells, Volume 93, Issue 2, February 2009, Pages 273-279, ISSN 0927-0248, 10.1016/j.solmat.2008.10.017.

[28] G. Conibeer, M. A. Green, D. König, I. Perez-Wurfl, S. Huang, X. Hao, D. Di, S. Shrestha, B. Puthen-Veetil, Y. So, B. Zhang, Z. Wan, Prog Photovolt: Res. Appl. In press, (2010).

[29] ARC PV center of excellence annual report, (2011) available online at http://www.pv.unsw.edu.au/research/annualreports.asp

[30] L. Ma, D. Lin, G. Conibeer and I. Perez-Wurfl, Phys. Status Solidi C, 1-4 (2010).

[31] Hao, X.J., Cho, E.-C., Scardera, G., Shen, Y.S., Bellet-Amalric, E., Bellet, D., Conibeer, G., and Green, M.A. Sol. Energy Mater. Sol. Cells, 93 1524-1530 (2009)

[32] Hao, X.J., Cho, E.-C., Flynn, C., Shen, Y.S., Park, S.C., Conibeer, G., and Green, M.A. Sol. Energy Mater. Sol. Cells, 93, 273279 (2009).

[33] G. Cantele, E. Degoli, E. Luppi, R. Magri, D. Ninno, S. Ossicini, Phys Rev. B, 69 (2004), 155411

[34] Seung Hui Hong, Yong Sung Kim, Woo Lee, Young Heon Kim, Jae Yong Song, Jong Shik Jang, Jae Hee Park, Suk-Ho Choi and Kyung Joong Kim, Active doping of B in silicon nanostructures and development of a Si quantum dot solar cell, Nanotechnology, 22, 425203, 2011.

[35] D. E. Aspnes. Optical properties of thin films. Thin Solid Films 1982; 89:249-262.

[36] J. G. E. Jellison, F. A. Modine. Parameterization of the optical functions of amorphous materials in the interband region.Appl. Phys. Lett. 1996; 69:371-3.

[37] H. Song, A. B. Sproul, A. G. Aberle. Doping dependence of optical properties of solid-phase crystallized evaporated poly-Si thin films on glass. Conference on Optoelectronic and Microelectronic Materials and Devices. COMMAD 2008; 293-6.

[38] S. K. Shrestha, P. Aliberti, G. Conibeer. Energy selective contacs for hot carriers solar cells. Sol. En. Mat. and Sol. Cells 2010; 94:1546-50

[39] M Lannoo, C Delerue, G Allan, Phys. Rev. Lett. 74, 17, 1995.

[40] David J. Norris,Alexander L. Efros,Steven C. Erwin, Doped Nanocrystals, Science 28 March 2008: 319 (5871), 1776-1779.

[41] D.K. Schroder, Semiconductor Material and Device Characterization, J. Wiley & Sons, ISBN 0-741-24139-3, 1998 and references therein

[42] G.K. Reeves, H.B. Harrison, Obtaining the Specific Contact Resistance from Transmission Line Model Measurements IEEE Electron Device Letters, Vol. 3, No. 5, p. 11 I , 1982.

[43] J.H. Klootwijk, C.E. Timmering, Merits and Limitations of Circular TLM structures for contact resistance determination for novel 111-V HBTs,Proc. fEEE 2004 Int. Conference on Microelectronic Test Structures, Vol 17, March 2004

[44] A.M. Sze, Physics of Semiconductors Devices, 1-763 (2007)

[45] W.R. Harrell, J. Frey, Observation of PooleFrenkel effect saturation in SiO2 and other insulating films, Thin Solid Films, Volume 352, Issues 1-2, 8 September 1999, Pages 195-204

[46] S. Johnson, A. Markwitz, M. Rudolphi, H. Baumann, S. P. Oei, K. B. K. Teo, and W. I. Milne, Field emission properties of self-assembled silicon nanostructures on n- and p-type silicon, Appl. Phys. Lett. 85, 3277 (2004)

[47] I. Perez-Wurfl, L. Ma, D. Lin, X. Hao, M.A. Green, G. Conibeer, Silicon nanocrystals in an oxide matrix for thin film solar cells with 492mV open circuit voltage, Solar Energy Materials and Solar Cells, Available online 4 May 2011, ISSN 0927-0248, 10.1016/j.solmat.2011.02.029.

[48] Ivan Perez-Wurfl, Xiaojing Hao, Angus Gentle, Dong-Ho Kim, Gavin Conibeer, Martin. A. Green, Si nanocrystal p-i-n diodes fabricated on quartz substrates for third generation solar cell applications, Appl. Phys. Lett. 95, 153506 (2009).